

**ThesisTitle**

by

**Daniel C. Cole**

Other Degrees

A thesis submitted to the  
Faculty of the Graduate School of the  
University of Colorado in partial fulfillment  
of the requirements for the degree of  
Doctor of Philosophy  
Physics Physics  
2018

This thesis entitled:  
ThesisTitle  
written by Daniel C. Cole  
has been approved for the Physics Physics

---

Reader1

---

Reader2

Date \_\_\_\_\_

The final copy of this thesis has been examined by the signatories, and we find that both the content and the form meet acceptable presentation standards of scholarly work in the above mentioned discipline.

Cole, Daniel C. (Ph.D., Physics)

ThesisTitle

Thesis directed by Dr. Scott A. Diddams

Optical frequency combs have revolutionized precision metrology by enabling measurements of optical frequencies, with implications both for fundamental scientific questions and for applications such as fast, broadband spectroscopy. In this thesis, I describe the development of comb generation platforms with smaller footprints and higher repetition rates, with the ultimate goal of bringing frequency combs to new applications in a chip-integrated package. I present two new types of frequency combs: electro-optic modulation (EOM) combs and Kerr-microresonator-based frequency combs (microcombs). First I describe the EOM comb scheme and, in particular, techniques for mitigating noise in the comb generation process, and I present the results of a proof-of-principle metrology experiment and some possible applications. Then I discuss developments in microcomb technology. I present novel soliton crystal states, which have highly structured fingerprint optical spectra that correspond to ordered pulse trains exhibiting crystallographic defects. These pulse trains arise through interaction of the solitons with avoided mode-crossings in the resonator spectrum. Next, I describe the direct and deterministic generation of single microresonator solitons using a phase-modulated pump laser. This technique removes the dependence on initial conditions that was formerly a universal feature of these experiments, presenting a solution to a significant technical barrier to the practical application of microcombs. I also discuss generation of Kerr combs in the Fabry-Perot (FP) geometry. I introduce a nonlinear partial differential equation describing dynamics in an FP cavity and discuss the differences between the FP geometry and the ring cavity, which is the geometry used in previous Kerr-comb experiments. Finally, I discuss a technique for reducing the repetition rate of a high-repetition-rate frequency comb, which will be a necessary post-processing step for some applications. I conclude with a discussion of avenues for future research, including the chip-integration of Fabry-Perot Kerr resonators and the use of band-engineered photonic crystal cavities to further simplify soliton generation.

## Acknowledgements

The work in this thesis would not have been possible...

- Acknowledgement line 1
- Acknowledgement line 2

## Contents

<b>1</b>	Soliton crystals in microresonators	<b>1</b>
1.1	Spectral and temporal characteristics of soliton crystals . . . . .	1
1.2	Soliton crystal generation . . . . .	3
1.3	Mechanism of soliton crystallization . . . . .	3
1.3.1	Simulation of soliton crystals . . . . .	5
1.4	Case study: pair distribution function for a superstructured crystal . . . . .	5
1.5	Soliton crystal configuration space . . . . .	7
1.6	Time-domain measurements of soliton crystals . . . . .	11
<b>2</b>	EOM Combs	<b>13</b>
2.1	Principle of operation . . . . .	13
2.2	Generation of an EOM comb and detection of its carrier-envelope offset frequency .	14
2.3	Noise considerations in EOM comb generation . . . . .	17
2.4	Outlook . . . . .	19
	<b>References</b>	<b>20</b>

## Figures

1.1	Spectral contrast of a soliton crystal . . . . .	2
1.2	Generation and characterization of a soliton crystal . . . . .	4
1.3	Stabilization and collapse of a soliton crystal . . . . .	6
1.4	Spectrum and waveform of a superstructured soliton crystal . . . . .	7
1.5	Simulated generation of a superstructured soliton crystal . . . . .	8
1.6	Pair distribution function for soliton crystal generation . . . . .	9
1.7	Taxonomy of soliton crystals . . . . .	10
1.8	Cross-correlation characterization of a soliton crystal . . . . .	12
2.1	Schematic and principle of operation for generation of a coherent octave-spanning EOM comb supercontinuum . . . . .	15
2.2	Figure Title . . . . .	16
2.3	Figure Title . . . . .	17
2.4	Figure Title . . . . .	18
2.5	Figure Title . . . . .	19

## List of Abbreviations

HRR	High repetition rate
DC	Direct current
RF	Radio frequency
IM	Intensity modulation
PM	Phase modulation
HNLF	Highly-nonlinear fiber
SMF	Single-mode fiber
SLM	Spatial light modulator
FWHM	Full-width at half-maximum
SPM	Self-phase modulation
DRO	Dielectric-resonator oscillator
SWAP	Size, weight, and power

# Chapter 1

## Soliton crystals in microresonators

This chapter presents results on the self-organization of ensembles of solitons in optical microring resonators. These results involve physics beyond the basic LLE model for Kerr-comb formation, as is described in Sec. 1.3. These experiments are performed using silica microrod [17] and microdisk [13] resonators with  $\sim 25$  GHz and  $\sim 16.5$  GHz FSR, respectively, but the principle applies to any resonator that supports multiple transverse modes. We refer to these self-organized soliton ensembles as ‘soliton crystals,’ which extends an analogy to condensed-matter physics that has been made in other nonlinear-optical systems, including single-pass nonlinear fiber systems [64] and harmonically mode-locked fiber lasers [65, 66], where a different mechanism for soliton crystallization that is based on two distinct timescales of the laser medium was identified [67]. It is interesting to note that the spatiotemporal chaos exhibited by Kerr combs was referred to as a ‘soliton gas’ in early studies of nonlinear dynamics in passive fiber-loop resonators [68–70].

### 1.1 Spectral and temporal characteristics of soliton crystals

Soliton crystals in Kerr resonators are soliton ensembles in which each soliton lies on a lattice site  $\theta_n = 2\pi n/N$  in the azimuthal co-moving frame, where  $N$  is a lattice parameter that arises from the fundamental physics of the system as described below and  $n$  indexes over the lattice sites. In the soliton crystals presented below there are many more available lattice sites than solitons, so that a fraction of the lattice sites are occupied. In the frequency domain, the temporal ordering of pulses in a soliton crystal corresponds to a highly modulated optical spectrum that exhibits distinctive features.

We present plots illustrating the spectral and temporal characteristics of an example soliton crystal in Fig. 1.1. Fig. 1.1a shows an experimental measurement of a soliton crystal spectrum. This spectrum exhibits prominent comb modes similar to primary-comb lines, and underlying these primary-comb lines are single-FSR-spaced spectral lobes. We can understand this spectrum through the basic superposition principle of the electric field: The primary comb spectrum with spacing  $N \times f_{FSR}$  corresponds to a train of  $N$  uniformly spaced pulses in the resonator; here  $N = 24$ . To this pulse train we add an *out-of-phase* pulse  $S_-$  that coincides in time with one of the existing pulses—in the time domain this corresponds to the introduction of a vacancy into the pulse train, while in the frequency domain this corresponds to the addition (in the phase-sensitive field quantity) of the primary-comb spectrum and the spectrum of the single, out-of-phase soliton. We then add a second soliton  $S_+$  to the pulse train, this one *in phase* with the existing pulses and slightly temporally shifted from the vacancy. The time-domain result is a pulse train with one pulse displaced from its expected position based on uniform spacing. In the frequency domain, the positions of the pulses  $S_+$  and  $S_-$  correspond to different linear spectral phase shifts on each of their individual spectra; when these spectra are added together the result is spectral interference that is periodic in frequency. This gives rise to the lobes beneath the primary-comb lines; the frequency period of the interference is inversely proportional to the separation between the pulses  $S_+$  and  $S_-$  in time.

We illustrate this principle by plotting pulse trains exhibiting a shifted pulse in Fig. 1.1b, and show their calculated spectra in Fig. 1.1a. These pulse trains are constructed using the analytical

approximation to soliton ensembles provided by Eq. ???. The pulse train shown in orange is composed of solitons pinned to sites on a lattice, and the pulse train shown in blue is obtained from this first pulse train by introducing a small random displacement to the position of each pulse. The effect of this small position jitter is apparent in the calculated spectra in Fig. 1.1a—the highly-distinctive spectral characteristics of the soliton crystal are eroded. In fact, it is a general property of the soliton-crystal spectra that we present in this chapter that the contrast and definition of the distinctive spectral characteristics depends on the high precision with which the pulses fall on the lattice sites.

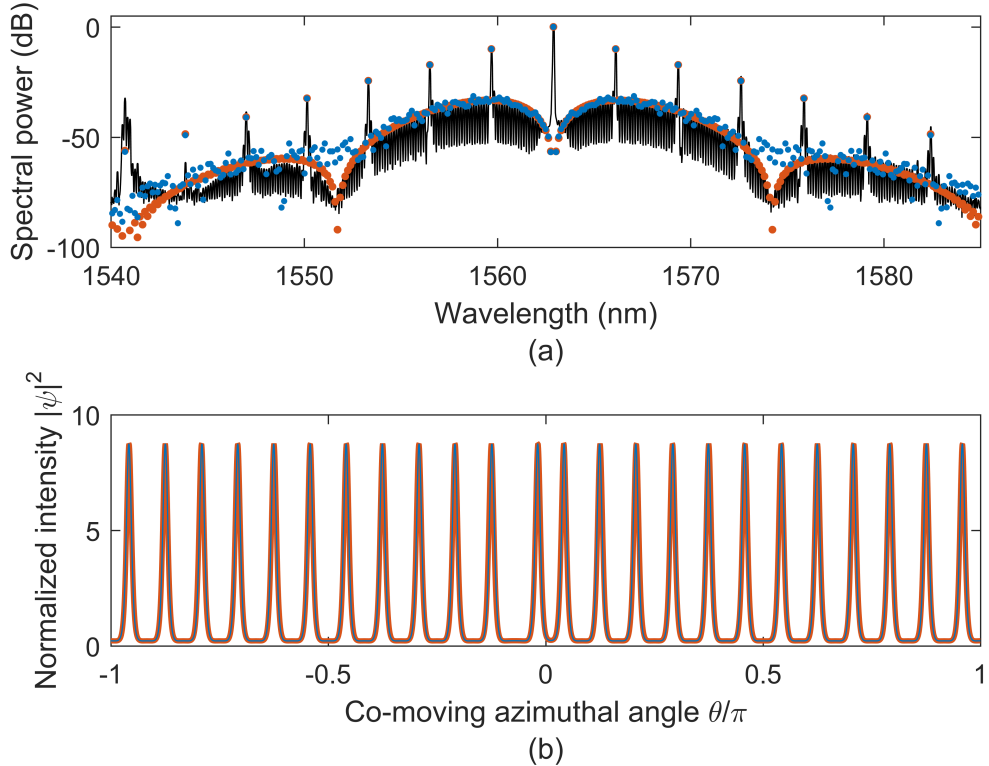


**Figure 1.1: Spectral contrast of a soliton crystal.** (a) Experimental measurement of a soliton-crystal spectrum (black), along with two approximations to the crystal’s time-domain waveform as a soliton ensemble, according to Eq. ???. Shown in orange is the spectrum of an ensemble of solitons pinned to sites on a lattice with spacing  $2\pi/(7 \times 24)$ ; here the majority of the pulses are separated from their neighbors by seven lattice sites, but one pulse is displaced by two lattice sites from its expected position. Shown in blue is a calculation of the spectrum that results when random (uniformly distributed) jitter is imposed on the same pulse positions; the range of the jitter is  $\pm 3\%$  of the typical inter-soliton spacing  $2\pi/24$ . (b) Time-domain traces corresponding to the spectra shown in (a). There is no readily apparent difference between the positions of the pulses in two pulse trains because the magnitude of the imposed jitter is small; nevertheless the definition of the distinctive spectral features is eroded by the jitter.

## 1.2 Soliton crystal generation

Soliton crystals are characterized by stable, dense occupation of the resonator by soliton pulses, and this dense occupation comes with high circulating power relative to single solitons or few-soliton ensembles. This important fact allows soliton crystals to be generated with decreasing pump-laser frequency scans across the resonance that are adiabatic—slow enough that both the resonator temperature and the state of the comb  $\psi$  are maintained at values<sup>1</sup> that correspond to the instantaneous  $\alpha$  and  $F^2$  parameters throughout the scan. We demonstrate generation of a soliton crystal in a slow scan in Fig. 1.2; it is interesting to contrast the continuity of the taper-transmission trace with the staircase-like nature of the same measurement exhibited in the generation of a few-soliton ensemble (see e.g. Ref. [29] and the discussion in Chap. ??). Slower scans than the one presented in Fig. 1.2 are possible, and in fact we have generated soliton crystals by tuning the pump-laser frequency arbitrarily slowly by hand.

## 1.3 Mechanism of soliton crystallization

The time-domain waveforms we have considered so far are not stable in evolution under the LLE. For each, the observed width of the spectrum fixes the ratio between  $\alpha$  and  $\beta$ , as seen from Eq. ???. This ratio then fixes the temporal duration of the solitons, in turn determining the characteristic length of their interactions. When an attempt to simulate the crystal according to the LLE is made with parameters that give agreement with the measured width of the optical spectrum (e.g.  $F^2=3.7$ ,  $\alpha = 3.77$ , and  $\beta = -0.0054$  for the crystal in Fig. 1.2c and d), it is found that pair-wise attractive interactions between solitons lead to collapse of the crystal, as shown below in Fig. 1.3.

A stabilization mechanism that goes beyond the physics of the LLE is responsible for the stability of soliton crystals. The stabilization mechanism for the crystals we present here arises from avoided mode crossings in the resonator spectrum. As discussed in Sec. ??, the resonators used in these experiments support multiple families of circulating modes, each with its own transverse spatial intensity profile and free spectral range. Although the modes in different families are in principle orthogonal, coupling between them can be provided by perturbations, for example by the coupling waveguide or tapered fiber used to drive the resonator, or anomalies in the resonator fabrication that break the resonator symmetry. When a coupling exists between modes that are sufficiently close in frequency, the modes become hybridized and their frequencies become displaced [71]. The effect of this coupling and the associated perturbation to the resonator mode spectrum on Kerr-comb generation has been investigated [Savchenkov2012], and it has been found that avoided mode crossings can inhibit soliton generation in anomalous-dispersion resonators [47, 72], while they can facilitate the formation of Kerr-combs in normal-dispersion resonators [Xue2015, Bao2017, 73].

Here we are interested specifically in the impact of an avoided mode crossing on the temporal waveform of a soliton. For simplicity, we make the approximation that a single mode of the Kerr comb with number  $\mu_x$  is affected by the mode crossing. This approximation neglects the fact that avoided mode crossings between two families typically span a range of modes as the mode frequencies traverse each other in frequency space due to a small fractional difference between the free-spectral ranges of the two mode families; this can be observed in many of the experimental spectra presented in this chapter. However, we find that the single-mode assumption is generally sufficient for modeling the stability of the soliton crystals that we observe.

The perturbation of the frequency of a resonator mode  $\mu_x$  that is far from the pumped mode  $\mu = 0$  affects the local detuning of the comb from the resonator. When this local comb-resonator detuning is decreased, the efficiency of nonlinear frequency conversion to mode  $\mu_x$  can be increased. This increases the amplitude of mode  $\mu_x$  in the soliton's spectrum, and the resulting change to the time-domain waveform can be understood by considering this increase as the addition of extra CW light at the frequency of mode  $\mu_x$ . This extra CW light leads to the introduction of periodic intensity oscillations in the background on which the soliton rides as it beats against the existing

modelocked  
dark pulse  
kerr combs,  
spatial mode  
interaction  
induced...,  
soliton gen-  
eration in  
overmoded  
resonators

<sup>1</sup> This terminology is a bit imprecise when applied to chaotic Kerr-combs that evolve with time; in this case the chaos exhibits the same behavior at each point in the scan that would be expected if  $\alpha$  and  $F^2$  were held fixed.

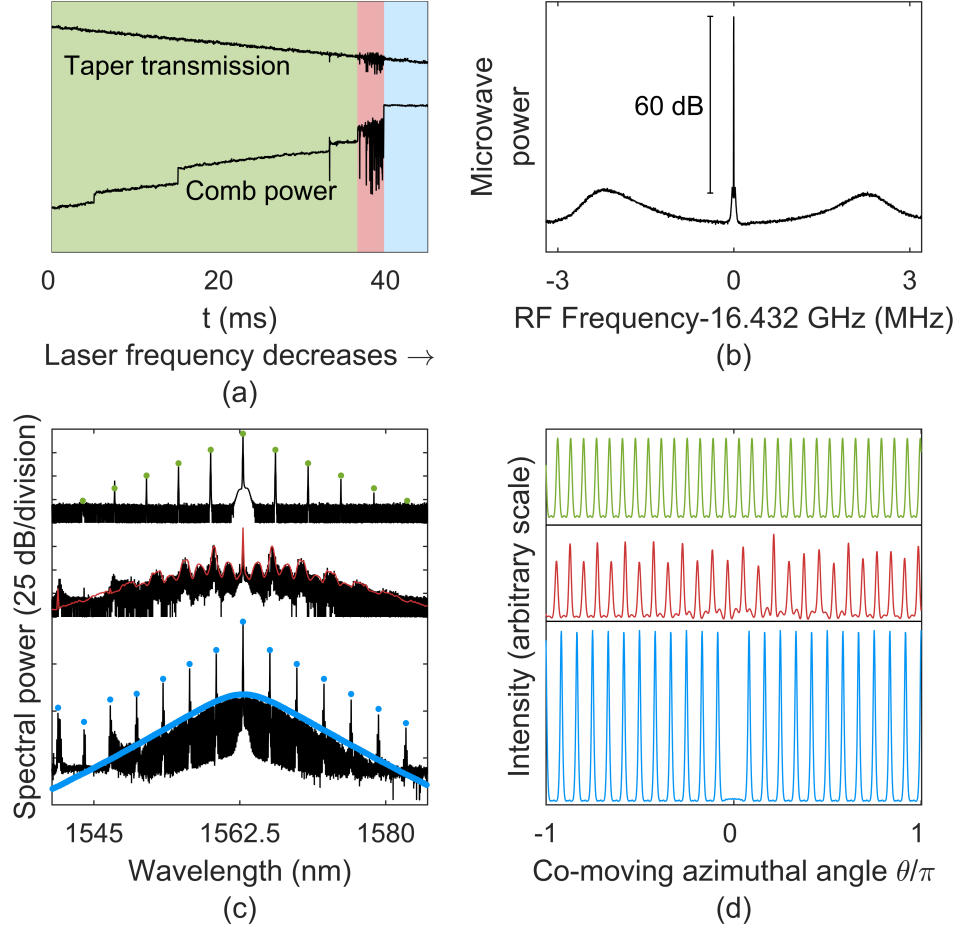


**Figure 1.2: Generation and characterization of a soliton crystal.** (a) Measurements of the power transmitted past the resonator ('Taper transmission') and this power with the pump frequency filtered out ('Comb power') during crystal generation with a scan that proceeds through primary-comb (green), chaotic (red), and soliton crystal (blue) regimes. The resonator's thermal response leads to the non-Lorentzian taper transmission profile, and the continuity of the taper transmission trace upon soliton crystal condensation indicates that the intracavity power of the soliton crystal is matched to the chaos that precedes it. (b) Narrow measured RF beat for the repetition rate of the soliton crystal is indicative of a coherent comb, in contrast with the chaotic state. (c) Progression of the optical spectrum through the scan, with experimental data (black) obtained by halting the scan at the appropriate point, and LLE simulations (with a perturbation as described in Sec. 1.3) in color. The simulated spectrum for the chaotic state shown in red is a time average. (d) Simulated time-domain traces corresponding to the simulated spectra in (c). The simulated intensity for the chaotic state is a snapshot. The soliton crystal shown in blue is a uniform pulse train with a single vacancy (see text).

background at the pump frequency. The new background wave in the cavity has a period of  $2\pi/\mu_x$  in the angular coordinate  $\theta$ .

When several of these perturbed solitons co-propagate in a resonator, they interact through their extended waves and arrange themselves such that the waves constructively interfere [44]. Each soliton then lies at the peak of a single extended background wave in the resonator, similar to

predictions for bichromatically pumped Kerr combs [74]. Importantly, temporal separations between solitons are therefore required to be multiples of this wave's period, and the wave stabilizes the crystal against the attractive interactions discussed above. Furthermore, the wave's amplitude, and thus the strength of the crystal against perturbations, increases with the number of co-propagating perturbed solitons. Within the assumption of single-mode perturbation of the comb's spectrum, this interaction has infinite range.

We note that the mechanism observed here builds on previous reports of related phenomena. It has been shown that local interactions between cavity solitons can arise through decaying oscillatory tails [75], leading to the formation of small, locally ordered soliton molecules; this effect appears to be significant in Kerr ring resonators only at small detunings [45]. Additionally, it has been shown that the injection of a second CW laser into a passive fiber-ring resonator can result in the generation of uniform distributions of solitons [76]. The mechanism we report here can be viewed as a variant of this CW-soliton interaction in which the ‘injected’ CW laser is provided by the solitons themselves through the effect of the mode crossing on the solitons' spectra.

We connect this discussion to the soliton-crystal spectrum presented in the bottom trace of Fig. 1.2c—this spectrum exhibits excess power near pump-referenced modes numbers  $\mu_{x,1} = 5 \times 24 = 120$  (1547 nm) and  $\mu_{x,2} = 7 \times 24 = 168$  (1541 nm), where 24 FSR is the spacing of the prominent primary-comb lines. Also visible is suppressed comb generation where the comb-resonator detuning has been increased.

### 1.3.1 Simulation of soliton crystals

To incorporate the stabilization mechanism described above into numerical simulations, we insert into the LLE a reduced comb-resonator detuning on a single mode  $\mu_x$ . The mode-dependent comb-resonator detuning can be calculated as:

$$\alpha_\mu = -2(\omega_p + \omega_\mu - D_1)/\Delta\omega_{tot}, \quad (1.1)$$

$$= \alpha - \beta\mu^2/2. \quad (1.2)$$

Here  $\Omega_0$  is the frequency of the pump laser,  $\omega_\mu$  is the set of cavity resonance frequencies referenced to the pumped mode, and  $D_1 = \partial\omega_\mu/\partial\mu|_{\mu=0}$  is the resonator's FSR at the pumped mode and is also assumed to be the comb's repetition rate. The dispersion operator is applied in the frequency domain in numerical simulations of the LLE (see ??), which facilitates inclusion of  $\delta$ -function perturbations to the comb-resonator detuning as:

$$\alpha_\mu = \alpha - \beta\mu^2/2 + \Delta\alpha_\mu, \quad (1.3)$$

where

$$\Delta\alpha_\mu = 2(\omega_\mu - \omega_{\mu,0})/\Delta\omega_{tot} \quad (1.4)$$

check math

is the normalized change in the frequency of mode  $\mu$  from the expected frequency  $\omega_{\mu,0}$ .

We demonstrate the stabilization mechanism and the simulation method by presenting a simulation of the crystal in Fig. 1.2c. The simulation is shown in Fig. 1.3. This figure illustrates both the rapid timescale over which the stabilization mechanism acts and the instability of the crystal in the absence of the stabilization mechanism. To explain the stability of this 23-soliton crystal and the apparently exact circumferential spacing of the pulses by  $2\pi/24$  radians, it is sufficient to incorporate into the LLE a reduced comb-resonator detuning on only mode 120 or on mode 168, where the excess power is largest. The crystal is then a steady-state solution of the resulting perturbed LLE.

## 1.4 Case study: pair distribution function for a superstructured crystal

We consider a third specific example of a soliton crystal. The measured and simulated optical spectra for this crystal are shown in Fig. 1.4a. This crystal exhibits superstructure—the soliton

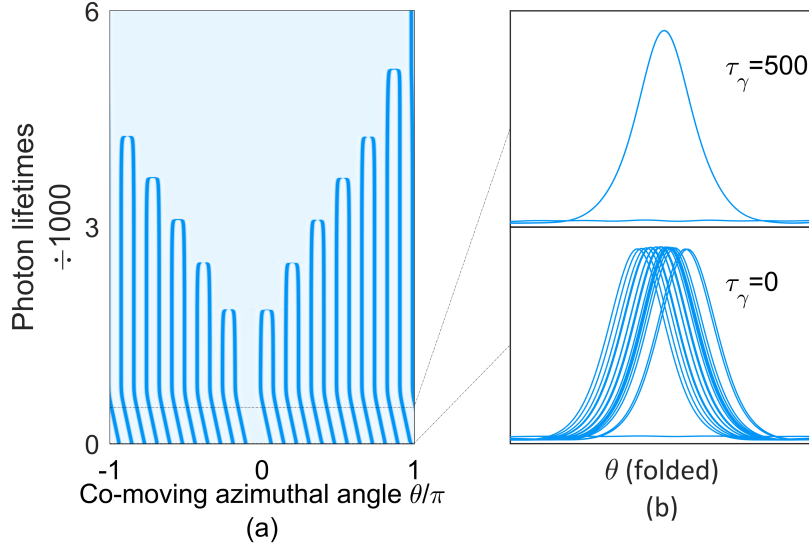


**Figure 1.3: Stabilization and collapse of a soliton crystal.** (a) Simulated evolution of the pulse train corresponding to the experimental crystal spectrum shown in Fig. 1.2c, starting from irregular pulse positions. For the first 500 photon lifetimes of the simulation, the propagation is governed by a perturbed LLE including reduced comb-resonator detuning on modes  $\mu_{\times,1} = 120$  and  $\mu_{\times,2} = 168$ . The soliton ensemble crystallizes within 10 seconds of initialization of the simulation, and then drifts within the co-rotating frame because the additional CW light on modes  $\mu_{\times,1}$  and  $\mu_{\times,2}$  corresponds to traveling waves. The reduced comb-resonator detuning is removed smoothly from 500 to 1000 photon lifetimes, resulting in the destabilization of the crystal and pair-wise annihilation of the solitons. (b) Intracavity power with the azimuthal coordinate folded modulo  $2\pi/24$ , demonstrating the initial irregularity of the pulse positions and the crystallized pulse train after 500 photon lifetimes.

pulse train is nearly periodic in a small unit cell but is modulated with a larger periodicity. This results from the frustrated uniform distribution of 16 solitons with allowed inter-soliton separations of  $2\pi n/49$  radians; one pair is spaced by  $4 \times 2\pi/49$  instead of  $3 \times 2\pi/49$  radians. Excess power is apparent in the spectrum at mode  $\mu_{\times} = 49$  (highlighted by the red circle in the plot), and we simulate this crystal phenomenologically by reducing the comb-resonator detuning on mode 49 so that the observed and simulated amplitudes of this mode agree. The total background wave that emerges as the sum of the waves from each constituent soliton, is visible in the plots of the simulated intensity in Fig. 1.4b and c.

To gain insight into crystal generation, we simulate laser frequency scans across the resonance that generate this crystal in the presence of the mode crossing on mode 49. Example scans are shown for the case without the mode crossing (green) and with it (blue) in Fig. 1.5. In both scans, solitons emerge from chaos as the frequency of the laser is decreased. In the presence of the mode crossing, they are generated with inter-soliton separations of  $2\pi n/49$  radians. A greater number of solitons emerge from chaos in the presence of the mode crossing, and this higher number helps to stabilize the crystal against thermal changes in the experiment. Further, upon continuation of the simulation, some of the solitons in the scan without the mode crossing interact attractively and pair-annihilate, while the crystallized ensemble resulting from the scan with the mode crossing remains stable indefinitely.

We investigate the pair-distribution function (PDF) for the soliton ensembles generated by these scans. The PDF is the probability that a soliton exists at position  $\theta_0 + \Delta\theta$  given that a different soliton exists at position  $\theta_0$ , normalized to the density. This is a useful metric to classify particle

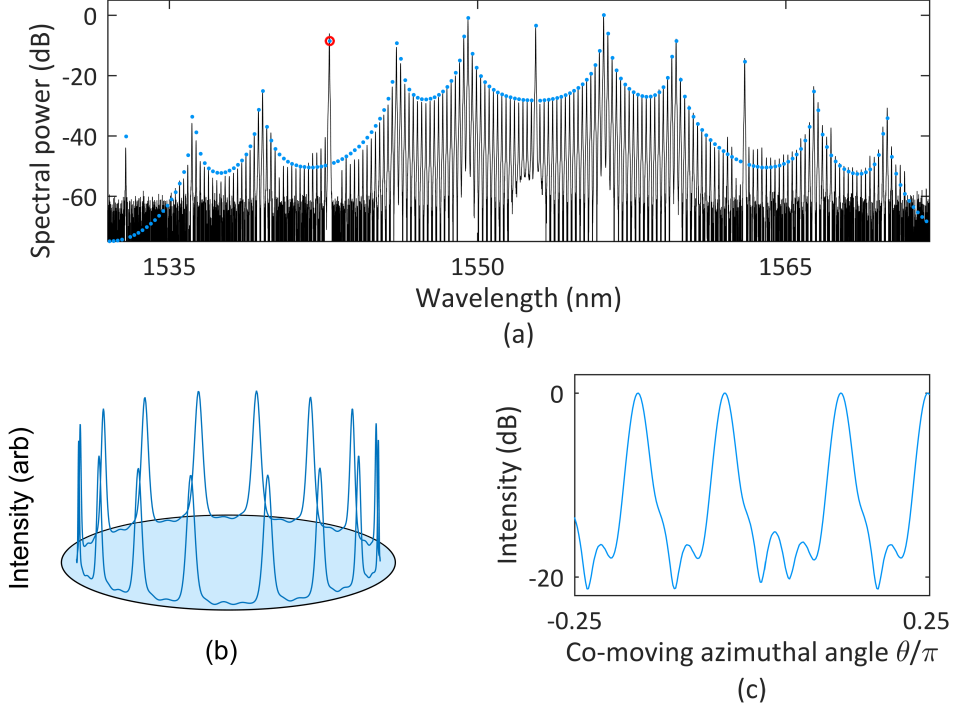


**Figure 1.4: Spectrum and waveform of a superstructured soliton crystal.** (a) Experimental (black) and simulated (blue) optical spectra of a superstructured crystal, with the red dot indicating the mode affected by a mode crossing as described in the text. (b) Simulated time-domain intensity of frustrated-uniform distribution of 16 solitons over 49 lattice points. (c) Zoomed-in logarithm-scale plot of the same that clearly shows unoccupied lattice sites and the anomalous  $4 \times 2\pi/49$  spacing between a pair of pulses.

interactions that we borrow from condensed matter physics (see e.g. Ref. [77], especially Fig. 2, and Ref. [78], especially Fig. 1.1 and Chapter 3). We note that for numerically calculated discrete PDFs the absolute scaling of the PDF is not important, as it depends on the density of numerical sampling. In Fig. 1.6, we plot the average PDFs for 10000 simulated scans with and without the mode crossing. The result for the case with a mode crossing is sharply peaked, indicating that the allowed inter-soliton separations take on discrete values. The result for the case without the mode crossing is continuous, with a peak near the most likely nearest-neighbour separation and periodic revivals at its multiples, falling to the value of the PDF for uncorrelated soliton positions (the density) at large separations. This is exactly the expected form of the PDF for a liquid [77, 78]. For comparison, we plot a PDF (black) generated by simulation of a simple particle ensemble with mean inter-particle separation of  $\Delta\theta = 0.155\pi$  and normally distributed noise on this value with standard deviation of  $\sigma_{\delta\theta} = 0.18\Delta\theta$ . Thus, with a particle labeled by  $n = 0$  fixed at  $\theta = 0$ , the position of particle  $n$  is  $\theta_0 = n\Delta\theta + \sum_n \delta\theta_i$ , with  $\delta\theta_i$  the instantiations of the random variable representing the noise on the pulse spacings. This simple model qualitatively matches the observed PDF for the simulations without the mode crossing.

## 1.5 Soliton crystal configuration space

We observe a rich variety of soliton crystals explained by ordering in accordance with an extended background wave as described above. Operationally, we adjust the pump laser power to

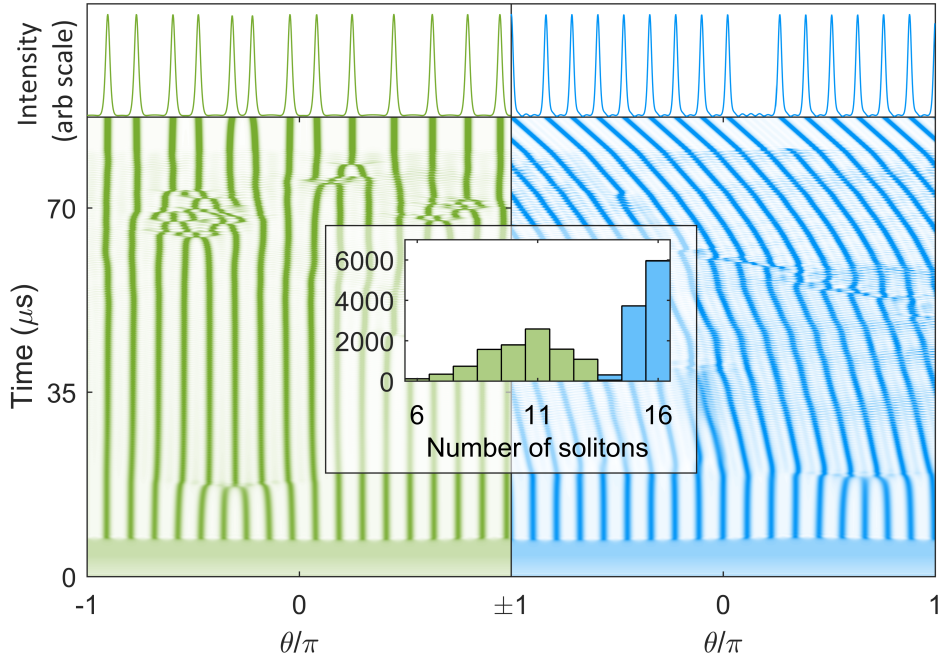


**Figure 1.5: Simulated generation of a superstructured soliton crystal.** Bottom: plots of the intracavity power during a simulated scan across the resonance, without (green) and with (blue) a mode crossing on mode 49 that reduces the comb-resonator detuning and increases the efficiency of frequency conversion on that mode. Top: final waveforms. Inset: histogram of the number of solitons generated in 10,000 simulated scans.

provide repeatable conditions for creating particular crystals; crystals exhibiting a greater number and variety of defects occur with increased laser power, which intensifies the fluctuations in the chaos that precedes crystal generation and provides less well-ordered initial conditions. Once a crystal is generated, it is stable to small adjustments in the pump power and detuning in accordance with the range of soliton existence shown in Fig. ??, as the crystal structure is determined by the initial conditions for soliton formation rather than by an explicit dependence on pump power or detuning.

Our interpretation of experimental data is based first on the fact that the LLE restricts the behavior of the field  $\psi$  to either an extended pattern (primary comb pulse train or chaos) or an ensemble of solitons. Simultaneous experimental measurement of 1. A quiet repetition-rate tone when the spectrum of the photodetected power is analyzed, and 2. Single-FSR spacing in the power spectrum indicate that a Kerr-comb is a soliton crystal<sup>2</sup>. To determine the temporal structure of a soliton crystal, we begin with the assumption that the spectrum corresponds to a soliton ensemble. Using the properties of the Fourier transform (e.g. linear superposition and the fact that a shift in time corresponds to a linear spectral phase shift), it is usually possible to deduce the configuration of pulses that must lead to the observed spectrum. Once the pulse train corresponding to the general structure of the spectrum has been deduced, the experimental spectrum can be compared to the spectrum of this pulse train calculated as an ensemble of solitons according to Eq. ???. This comparison reveals localized excess power in the experimental spectrum, which is evidence

<sup>2</sup> These requirements are probably sufficient, but not necessary—for example, a defect-free crystal will exhibit multi-FSR spacing. Experimentally, the difference between such a crystal and a primary-comb pulse train lies in the parameters  $\alpha$  and  $F^2$  that place the pump laser *either* in the regime for solitons or the regime for primary comb. However, these parameters are not necessarily straightforward to determine.

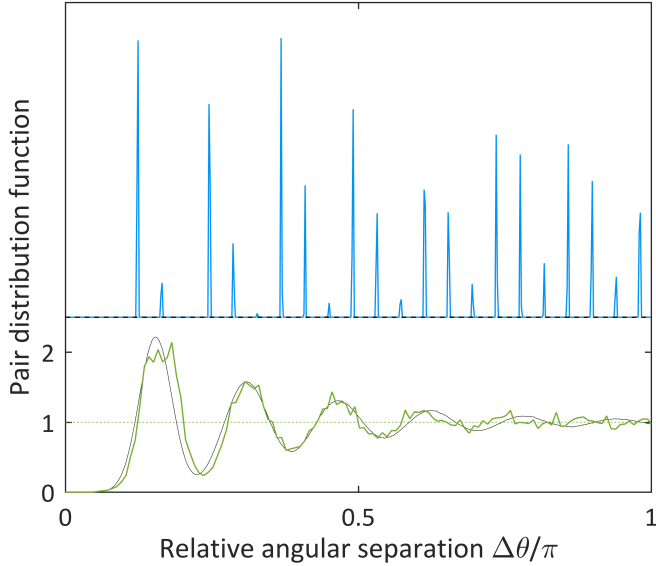
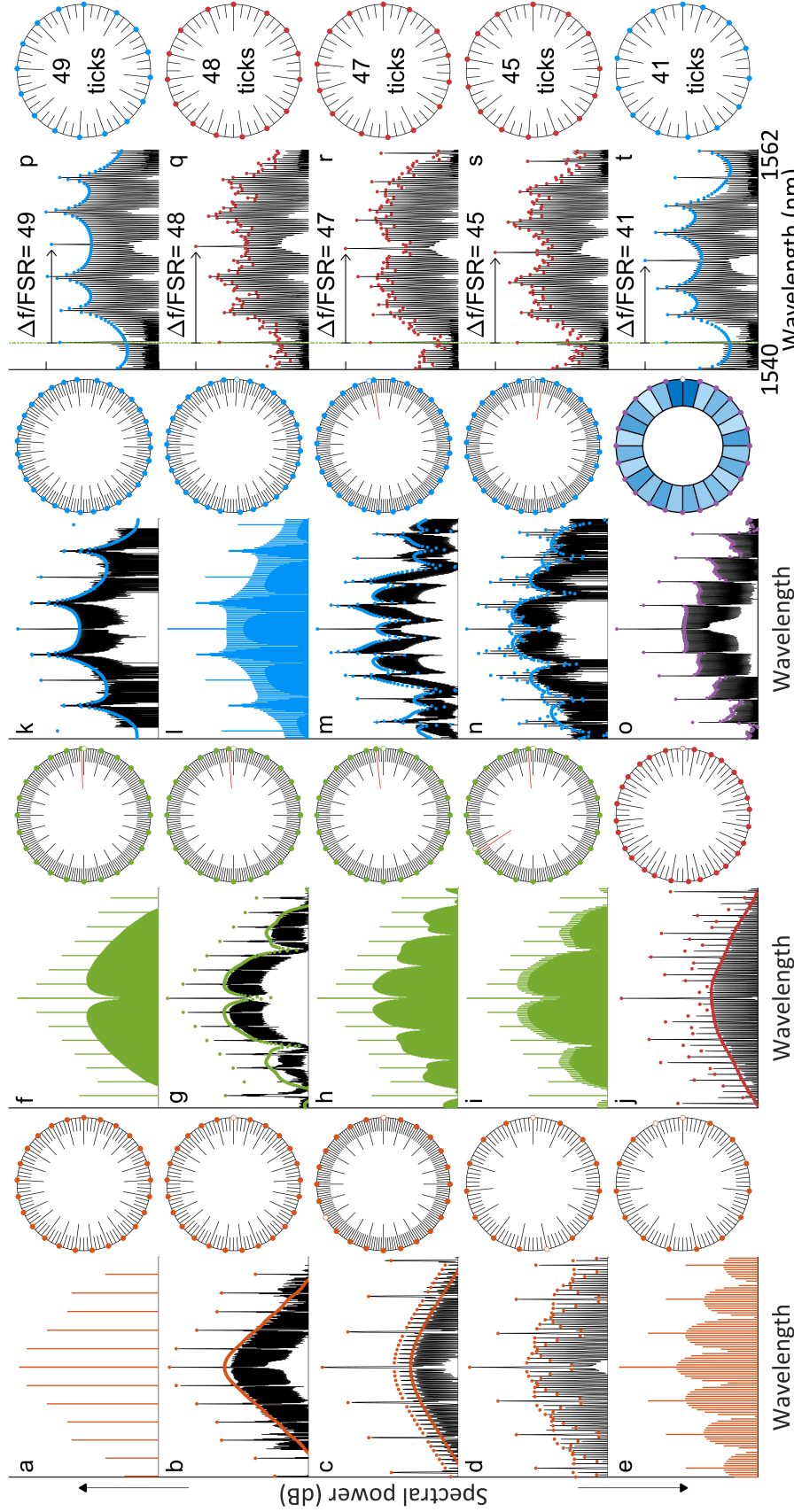


Figure 1.6: **Pair distribution function for soliton crystal generation.** Average pair-distribution functions calculated over 10,000 simulated scans across the resonance with (blue) and without (green) a mode crossing on mode 49. The width of the peaks in the discrete PDF is a single  $\Delta\theta$  bin. The expected PDF of a simple one-dimensional soliton liquid (see main text) is plotted for comparison in black.

of a mode crossing. The strength of the mode crossing, controlled in the experiment by e.g. the taper-induced coupling between modes, is determined phenomenologically from the magnitude of the excess power and reduced comb-resonator detuning on a single mode is incorporated into a perturbed LLE as described in Sec. 1.3. It is then verified that the pulse train whose spectrum matches the experimental data is a steady-state solution to this perturbed LLE, which requires the inter-soliton separations to be multiples of the period of the beat between the excess power and the pump laser. This period is  $2\pi/\mu_x$ , where  $\mu_x$  is the mode number of the affected mode. Because this process connects the presence of excess power on a single optical mode of the Kerr-comb spectrum to the general shape of the spectrum, two observations that are not related a priori, it provides strong evidence that the time-domain waveform of the crystal has been determined correctly.

The crystals we observe exhibit vacancies (Schottky defects), dislocations (Frenkel defects), disorder, or superstructure, or some combination thereof [79]. In a disordered crystal, the solitons still occupy lattice sites whose positions are determined by an avoided mode crossing in the resonator spectrum, but their distribution over these lattice sites varies without any apparent regular order or favored period. In this case, it is less straightforward to determine the pulse configuration from the shape of the spectrum. Instead, to determine the pulse configuration for a disordered crystal, we first identify excess power due to a mode crossing through observation of an asymmetry in the spectrum about the pump. The location of the excess power then fixes the allowed inter-soliton separations in the resonator, after which an exhaustive search is performed until a pulse train is found that yields the experimental spectrum.

Optical spectra for various observed and hypothetical soliton crystals are plotted in Fig. 1.7. We have simulated 13 of the experimental spectra as steady-state solutions to a perturbed LLE (this excludes crystal o); for 10 of these, the stabilizing mode crossing is visible in the data but not necessarily shown in the figure. For the other three the position of the mode crossing is inferred from the distribution of solitons and other crystal states observed in the same resonator.



**Figure 1.7: Taxonomy of soliton crystals.** Measured optical spectra are shown in black, with simulations in color. Schematic depictions of the soliton distribution in the resonator co-moving frame are shown to the right of each spectrum. Major ticks in the schematic diagrams indicate the location or expected location of a soliton. Minor ticks indicate lattice sites, corresponding to peaks of the extended background wave due to a mode crossing. (a) A perfect soliton crystal, consisting of 25 uniformly-distributed solitons. (b-e) Soliton crystals exhibiting vacancies. (f-i) Soliton crystals exhibiting Frenkel defects. Shifted solitons still occupy a lattice site. (j) A disordered crystal. (k-n) Crystals exhibiting superstructure. (o) A crystal with irregular inter-soliton spacings. Darker shading indicates a smaller inter-soliton spacing. The range in inter-soliton spacings is 3 % of the mean. (p-t) A series of crystals generated as the pump laser is moved progressively closer to the stabilizing mode crossing.

We highlight the crystal plotted in Fig. 1.7n. This crystal exhibits both superstructure, with a superlattice period of  $2\pi/3$  radians, and a Frenkel defect. Three identical supercells per resonator round-trip yield a spectrum which has light in optical modes spaced by three resonator FSR, because the waveform's period has been reduced threefold. The Frenkel defect, occurring once per round-trip, transfers a pulse from one supercell to another and contributes the single-FSR lobes to the spectrum. The result is three bursts of pulses containing 8, 9, and 10 solitons respectively.

Fig. 1.7o shows a soliton crystal with inter-soliton separations that are slightly irregular and that we have not simulated as a steady-state solution of any perturbed LLE. We expect that the formation of the crystal and the distribution of solitons are dictated by mode interactions, but that in this case our simple approximation of a perturbation to the LLE by a reduced comb-resonator detuning on a single comb mode is not appropriate.

Finally, we highlight the series of crystals plotted in Figs. 1.7p-1.7t. This series of crystals was generated by moving the pump laser closer to a mode-crossing in steps of integer multiples of the resonator FSR. This data demonstrates the influence of the background beating between the pump laser and the mode crossing in determining the configuration of solitons in the resonator.

I could change  $\Delta f$  to  $\Delta\nu$  on the figure.

## 1.6 Time-domain measurements of soliton crystals

It is recognized in ultrafast optics that it is not generally possible to infer the time-domain waveform of an optical signal from its optical power spectrum without additional information [80], because the spectrum contains no phase information. The LLE imposes restrictions on the possible time-domain field behaviors that can be exhibited, which can allow educated guesses to be made about the time-domain field based on the recorded optical spectrum, and we have been successful in modeling the observed spectra presented above as soliton ensembles. However, it is useful to confirm the LLE-assisted interpretation of experimental data both to strengthen the case for the LLE as a useful model for the system and to stay alert to the possibility of extra-LLE phenomena.

To verify our time-domain interpretation of the spectra we record in experiment, we characterize the temporal intensity of soliton crystals using an optical cross-correlation measurement. A depiction of the approach and the results for measurement of the time-domain intensity of the crystal shown in Fig. 1.7j is shown in Fig. 1.8. We send the Kerr-comb output and an optical reference pulse train through a LiIO<sub>3</sub> crystal with a relative angle of 90° between the beams. When the beams overlap in the crystal an amount of light proportional to the product of their intensities, at the sum of their frequencies, is emitted in a third direction. By measuring the average power of this emitted light while scanning the relative delay between the two beams, we measure the intensity cross-correlation between the crystal and the reference pulse.

In the limit of a  $\delta$ -function reference pulse, optical cross-correlation directly measures the time-domain waveform of an unknown signal. To approximate this limit, we perform cross-correlation measurements with a train of reference pulses that have duration comparable to that of the solitons, which allows us to precisely characterize soliton crystals. The reference pulse train is derived through electro-optic modulation (see Chapter ??) from the same laser that pumps the resonator, and the repetition rate of the reference pulse train is locked to the repetition rate of the Kerr-comb output.

We generate crystals in a through-coupled configuration, which results in interference between the out-coupled solitons and the through-coupled pump that depends on the coupling condition and that effects the time-domain waveform that propagates away from the resonator. In this particular experiment the out-coupled solitons destructively interfere with the through-coupled pump, with the result that the solitons manifest as dips in the through-coupled intensity. To correct this, before cross-correlation we use a spatial light modulator to rotate the phase of the pump laser by  $\pi$  so that it constructively interferes with the solitons, yielding solitons riding on top of a CW background.

The cross-correlation of the disordered crystal shown in Fig. 1.7j with the reference pulse train confirms our interpretation of the spectral data for this crystal. Fig. 1.8b shows the simulated time-domain waveforms of the reference pulse and the crystal, and Fig. 1.8c shows measured and simulated cross-correlation signals. The temporal spacing between the peaks of the cross-correlation

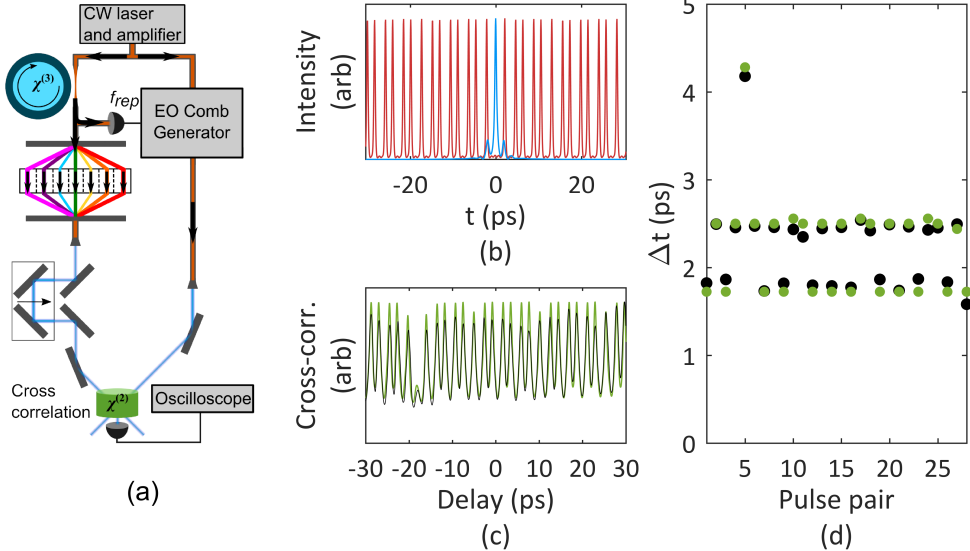


**Figure 1.8: Cross-correlation characterization of a soliton crystal.** Schematic depiction of the setup for using an electro-optic (EO) modulator comb as a reference pulse to measure the time-domain waveform of a soliton crystal. The  $\chi^{(3)}$  (Kerr) and  $\chi^{(2)}$  nonlinearities are indicated on the resonator and nonlinear crystal (LiIO<sub>3</sub>). A spatial light modulator is used to rotate the phase of the pump laser by  $\pi$  after crystal generation to compensate for interference between the out-coupled soliton crystal and the through-coupled pump light. The soliton crystal and the EO modulator comb share a pump laser, and the repetition frequency  $f_{rep}$  of the EOM comb is locked to that of the crystal. Varying the relative delay in one arm of this interferometer enables measurement of the intensity cross-correlation between the soliton crystal and the reference pulse. (b) Simulated crystal (red) and reference (blue) intensity profiles. (c) Measured (black) and simulated (green) cross-correlation signals. The contrast between peaks of the cross-correlation signal, for both theory and experiment, is limited by the duration and shape of the reference pulse and increases between soliton pairs with larger temporal separations. (d) Temporal separations between adjacent peaks for the measured (black) and simulated (green) cross-correlation signals. Mean fractional error is 3.5 %.

signals is shown in Fig. 1.8d, where a high degree of agreement between the data and the simulation is observed.

The simulated cross-correlation signal is sensitive to the intensity profile of the reference pulse. We can measure only its intensity autocorrelation, which we combine with our knowledge of its production to estimate the intensity profile. To demonstrate that the validity of the results we present here is not sensitive to the exact assumptions we make about the intensity profile, we have also simulated the intensity cross-correlation resulting from an assumed Gaussian reference pulse with the same autocorrelation width as is measured for the reference pulse. The resulting simulated cross-correlation does not qualitatively agree as well with the experimental data in the depths of the wells between peaks because it does not contain satellite pulses which contribute to the variations in this depth, but the quantitative comparison of the temporal spacing between peaks is similar: the mean (maximum) normalized error between experiment and theory is 3.5 % (9.1 %) for the assumed electro-optic comb pulse and 4.8 % (10.6 %) for the Gaussian pulse.

## Chapter 2

### EOM Combs

In this chapter, I discuss the generation of high-repetition-rate frequency combs through electro-optic modulation of a continuous-wave laser—so-called EOM combs [81–90]. This scheme represents an alternative to parametric generation of high-repetition-rate combs in Kerr resonators, and as the technology matures it will likely find a niche in the application space that leverages its long-term stability, lack of moving parts, and possibility for robust turn-key operation. First I present the operational principle, followed by experimental results that represent the first  $f - 2f$  self-referencing of a comb of this kind. Then I provide a discussion of the noise processes specific to the EOM comb, the investigation and mitigation of which is a significant contribution of the work described here. I conclude with a brief outlook for the technology.

#### 2.1 Principle of operation

At its simplest, an EOM comb is a set of lines generated by passing a CW ‘seed’ laser through cascaded phase and intensity modulators to generate a train of chirped pulses. After this initial step, the pulse train may be propagated through a dispersive medium to temporally compress the pulses, and they can be subsequently spectrally broadened. A generic expression for the electric field before temporal compression results from the product of the field  $E_o e^{-i\omega_c t}$  with operators

$$\frac{e^{i\Phi(t)} + e^{-i\Phi(t)}}{2} = \cos \Phi(t) \quad (2.1)$$

where

$$\Phi(t) = \phi_{DC} + \phi_{RF} \sin(\omega_{rep}t + \phi_{IMPM}) \quad (2.2)$$

representing the intensity modulation and

$$\exp[i\delta_{PM} \sin \omega_{rep}t] \quad (2.3)$$

representing the phase modulation. Here  $E_o$  and  $\omega_c$  are the complex amplitude and the carrier frequency of the seed laser. The phases  $\phi_{DC}$  and  $\phi_{RF}$  represent the DC bias and depth of the intensity modulation, respectively, which experimentally are sourced from a DC power supply and an RF synthesizer. Writing the intensity-modulation operator as the sum of exponentials reveals the physical origin of intensity modulation as phase modulation in two paths with opposite sign. The phase-modulation index, which sets the initial bandwidth of the EOM comb, is  $\delta_{PM}$ . The comb’s repetition rate is  $f_{rep} = \omega_{rep}/2\pi$ , with  $\omega_{rep}$  the angular frequency of the phase and intensity modulation. In practice it is useful to derive these signals from the same synthesizer. The phase  $\phi_{IMPM}$  represents a phase difference between the IM and PM operators arising from path-length differences, which can be controlled via the insertion of a phase shifter in one electrical path.

For convenient temporal pulse compression and subsequent spectral broadening of the comb it is desirable to configure the IM and PM to yield a train of 50 % duty-cycle pulses with normal chirp (temporally increasing carrier frequency). To achieve this, both  $\phi_{DC}$  and  $\phi_{RF}$  are set to  $\pi/4$  and  $\phi_{IMPM}$  is set to zero. Experimentally, one can determine that the appropriate RF drive

power and bias have been applied by adjusting the ratios  $\eta_1 = P_1/P_0$  and  $\eta_2 = P_2/P_0$  between the first- and second-order sidebands and the carrier to  $\eta_1 =$  and  $\eta_2 =?$  with only intensity modulation applied to the seed laser<sup>1</sup>. Setting  $\phi_{IMPM}$  to either zero or  $\pi$  is achieved by examining the optical spectrum of the EOM comb with both IM and PM applied. The spectrum is asymmetric if  $\phi_{IMPM}$  is not zero or  $\pi$  due to stronger transmission of either the high- or low-frequency components of the phase-modulated seed laser through the intensity modulators. The optical spectrum of the comb, which does not include phase information, is the same for  $\phi_{IMPM} = 0$  or  $\pi$ ; the difference between the two corresponds to reversal of the field in time or, equivalently, the difference between normal and anomalous chirp. Setting  $\phi_{IMPM}$  to zero is accomplished by verifying that the pulses are compressed by propagation in an appropriate length of an anomalously dispersive medium;  $\phi_{IMPM} = \pi$  corresponds to anomalous chirp on the initial pulse train, in which case the pulses will not be compressed.

insert  
finish

A simplified and illuminating expression for the electric field of a normally-chirped 50 % duty-cycle pulse train (up to a constant overall phase shift relative to the previous expression) is:

$$E = E_o \cos\left(\frac{\pi}{2} \sin^2 \frac{\omega_{rep}t}{2}\right) e^{i\omega_c t - i\delta_{PM} \cos \omega_{rep}t}. \quad (2.4)$$

This can be understood as the product of a time-varying real amplitude  $a(t) = E_o \cos\left(\frac{\pi}{2} \sin^2 \frac{\omega_{rep}t}{2}\right)$  and a phase factor from which the instantaneous carrier frequency  $\omega(t) = \omega_c + \omega_{rep}\delta_{PM} \sin \omega_{rep}t$  can be calculated. The carrier frequency  $\omega(t)$  is increasing when the amplitude  $a(t)$  is at its maximum, corresponding to normal chirp on the pulses.

## 2.2 Generation of an EOM comb and detection of its carrier-envelope offset frequency

Here I describe the generation of an EOM comb with 10 GHz repetition rate and subsequent measurement of its carrier-envelope offset frequency. One advantage of the EOM comb scheme is that the generation and spectral broadening of the comb is well understood, and can be modeled accurately. To demonstrate this, I compare the results of simulations of the comb to the experimental output at each stage in the generation process.

The experimental setup is depicted in Fig. 2.1a. The basic experimental scheme consists of the following steps: 1. Initial generation and temporal compression of the EOM comb pulse train; 2. Modest spectral broadening and temporal re-compression; 3. Noise reduction using a Fabry-Perot filter cavity; and 4. Octave-spanning supercontinuum generation and detection of the carrier-envelope offset frequency. To my knowledge, the results described below represent the first time a frequency comb of this kind has been self-referenced. Key to the success of this approach is the implementation of nonlinear spectral broadening in two stages, which allows the second stage to be seeded with  $\sim 130$  fs pulses for coherent supercontinuum generation. Noise reduction with the Fabry-Perot filter cavity is also critical for coherent spectral broadening; I describe a characterization of this step below.

To generate the initial train of chirped pulses, a telecommunications-band CW laser is passed through cascaded phase and intensity modulators driven with a 10 GHz microwave signal. The intensity modulator is biased at the 50 % transmission point and driven with an RF amplitude appropriate for generation of a 50 % duty-cycle pulse train, as described above; the phase modulator is driven with modulation depth of  $\sim 31\pi/4 \sim 24.3$  rad. The relative phase between the modulators is set such that the phase applied by the phase modulator is at a minimum when the transmission of the intensity modulator is highest; this yields a train of normally-chirped (up-chirped) pulses. Simulated temporal intensity and instantaneous carrier-frequency profiles are shown in Fig. 2.1b, and a simulated optical spectrum is overlaid on an experimental measurement in Fig. 2.1c.

---

<sup>1</sup> This assumes that the modulation is applied to both paths in the intensity modulator with opposite sign; the correct ratios for single-path modulation can be calculated instead if required. To determine the internal configuration of the modulator, one can verify the action of the bias: if the modulation is applied to both paths with opposite signs, the bias will adjust only the ratios..., but if the modulation is applied to one path, ...

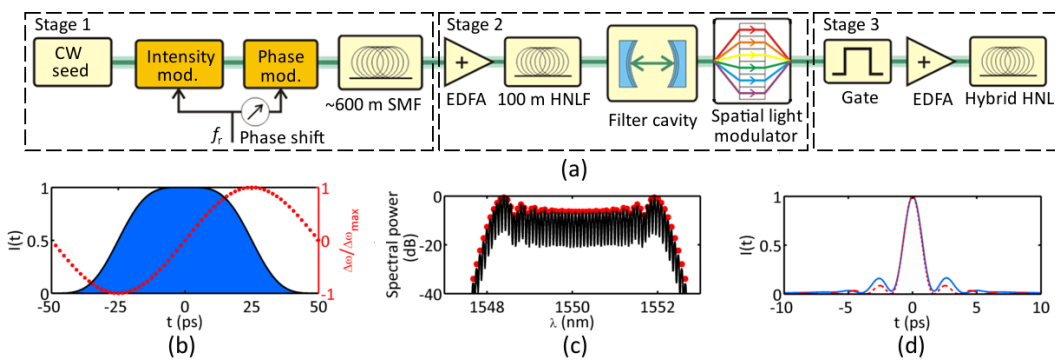


**Figure 2.1: Schematic and principle of operation for generation of a coherent octave-spanning EOM comb supercontinuum.** (a) Experimental schematic for supercontinuum generation, with three stages: 1. Initial generation and temporal compression of the pulse train; 2. First stage of spectral broadening and temporal re-compression, along with a filter cavity for noise suppression, and 3. Final stage of spectral broadening for generation of a coherent octave-spanning supercontinuum, including the implementation of an electro-optic gate for repetition-rate downsampling. (b) Depiction of a constituent pulse from a train of 50 % duty-cycle normally-chirped pulses with 10 GHz repetition rate. Intensity is shown in blue, and instantaneous carrier frequency is shown in red. The periodic electric field of this pulse train is given by Eqn. 2.4. (c) Measured optical spectrum of the initial EOM comb pulse train (black), along with the simulated spectrum corresponding to the plots in panel (b). (d) Simulated temporal compression of the pulses shown in panel (b), with compression conducted by propagation in 570 m of SMF (solid blue) and compression to the transform limit (dashed red). The full-width at half-maximum (FWHM) duration of both pulses is  $\sim 1.5$  ps.

Next, the chirped pulse train is propagated through 600 m of anomalously-dispersive SMF. The length of SMF that is appropriate for pulse compression depends on the bandwidth of the optical pulses to be compressed; equivalently, it depends on both the phase-modulation depth and the repetition rate of the pulse train. This temporal compression reduces the duration of the optical pulses from  $\sim 50$  ps to  $\sim 1.5$  ps. A simulation of the resulting intensity profile is presented in Fig. 2.1d.

The compressed pulses are amplified to 400 mW average power in an erbium-doped fiber amplifier and launched into 100 m of HNLF. This section of HNLF has chromatic dispersion that is small and normal; this is carefully chosen to chirp the pulses via self-phase modulation while avoiding soliton-fission dynamics[91]. The result is a train of chirped  $\sim 1.5$  ps pulses exiting the fiber. In Fig. 2.2a we present the measured optical spectrum of this pulse train, as well as results of a numerical simulation of the spectral broadening in the 100 m of normally-dispersive HNLF. These simulations are conducted using the nonlinear Schrodinger equation (NLSE) including third order dispersion[15], taking as initial conditions the calculated intensity profile of the EOM comb pulses shown in Fig. 2.1d. The dispersion values for the HNLF used in the simulation are  $D = -0.04$  ps/nm·km and  $D' = 0.003$  ps/nm<sup>2</sup>·km, close to the values specified by the manufacturer. The simulation method is described in detail in App. ??.

After propagation through the first section of HNLF, the pulses are passed through a high-finesse Fabry-Perot cavity for suppression of optical frequency fluctuations as discussed below. Then the pulses are temporally compressed again, this time using a commercial spatial light modulator (SLM) [92]; the SLM separates narrow spectral regions using a grating and passes them through individually controlled delaying elements before recombination. The SLM applies 2<sup>nd</sup>, 3<sup>rd</sup>, and 4<sup>th</sup> order chromatic dispersion, which simulations indicate is sufficient to compress the chirped pulses to  $\sim 130$  fs, near their transform limit. This is shown in Fig. 2.2b. While it is convenient, the

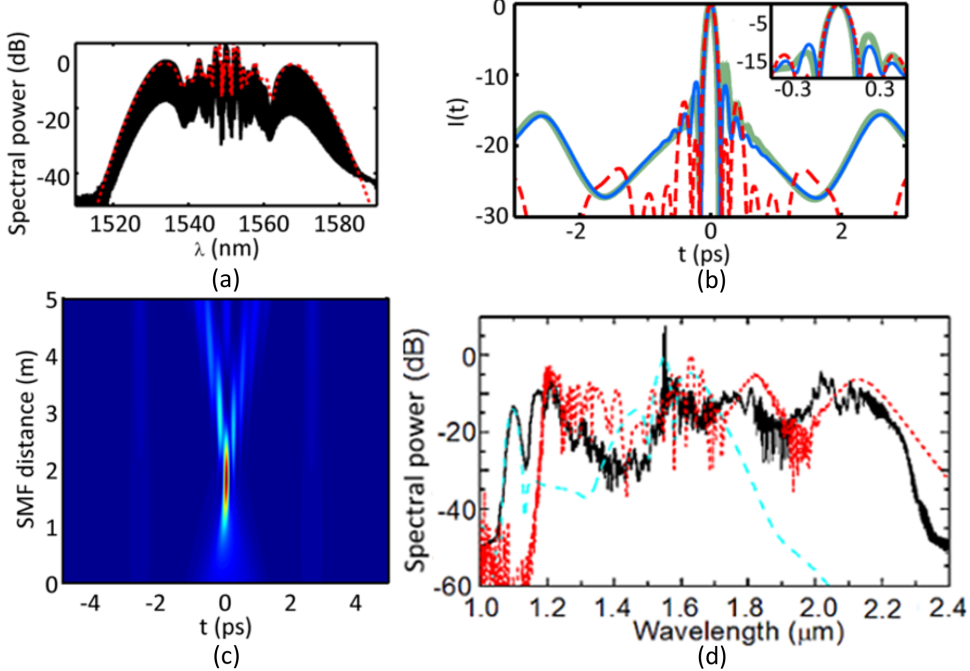


**Figure 2.2: Spectral broadening for generation of an octave-spanning supercontinuum.** (a) Measured optical spectrum after propagation in 100 m of low-normal-dispersion HNLF (black). The spectrum is broadened by self-phase modulation, which imposes a chirp on the pulses. Shown in red is a simulation of the same, conducted as described in the text. (b) Logarithmic-scale plot of the simulated pulse intensity envelopes after temporal recompression in the SLM with 2<sup>nd</sup>-, 3<sup>rd</sup>-, and 4<sup>th</sup>-order dispersion (blue), in an appropriate length of SMF (thick green), to the transform limit (dashed red). (c) Simulated re-compression of the SPM-chirped pulses (red spectrum in panel (a)) in SMF. (d) Measured optical spectrum of the octave-spanning supercontinuum generated by the EOM comb system (black), plotted along with simulated spectra calculated as described in the text to investigate the effects of the 30 cm, highly-dispersive piece of HNLF (long-dashed teal) and the 7.7 m, lower-dispersion piece of HNLF (short-dashed red).

SLM is not strictly necessary; it would also be possible to compress the pulses via propagation in an appropriate length of SMF. Figs. 2.2b and c present the output intensity profile and the evolution of the intensity profile, respectively, in simulated compression in SMF. Because the pulses are broadband, temporally short, and reasonably high energy, these simulations include the full dispersion profile of SMF and the Kerr nonlinearity.

The temporally compressed  $\sim$ 130 fs pulses are then passed through a Mach-Zehnder modulator functioning as an electro-optic gate for repetition-rate downsampling (see Chapter ??). The gate selectively transmits every fourth pulse, reducing the repetition rate of the pulse train to 2.5 GHz. This facilitates coherent supercontinuum generation in a second stage of spectral broadening by increasing the pulse energy that can be achieved at a given average power. Note that this step is convenient but not strictly necessary, as shown in Ref. [93].

The downsampled 2.5 GHz pulse train is amplified to an average power of 1.4 W, resulting in a train of  $\sim$ 0.56 nJ pulses. This pulse train is propagated through 8 m of hybrid HNLF, yielding the spectrum shown in Fig. 2.2d. This hybrid HNLF consists of two segments with different dispersion profiles, with each segment serving a different purpose. The first segment is 30 cm long and highly dispersive ( $D = 6 \text{ ps/nm}\cdot\text{km}$ ), and generates a dispersive wave centered at 1090 nm. The second segment is 7.7 m long and has lower dispersion ( $D = 1.5 \text{ ps/nm}\cdot\text{km}$ ), and generates a Raman-self-

frequency-shifted soliton centered near 2150 nm. The effect of each of these fibers on the output spectrum can be understood by investigating propagation in each section separately. To do this we use the LaserFOAM program [94], which employs the generalized NLSE including Raman scattering, self-steepening, and 2nd- through 4th-order dispersion. The simulations are run independently, and both take as their initial conditions 170 fs Gaussian pulses with 350 pJ energy, close to the energy coupled into the HNLF after accounting for losses. The results of these simulations are plotted in Fig. 2.2d.

The supercontinuum generated in the hybrid HNLF is coherent and suitable for  $f - 2f$  self-referencing. To detect the carrier-envelope offset frequency of the EOM comb, we pass the pulse train through an interferometer consisting of a dichroic mirror, a delay stage in one path, and a 10 mm sample of periodically-poled lithium niobate that generates the second harmonic of supercontinuum light at 2140 nm. The dichroic mirror and delay stage enable adjustment of the relative timing between the native 1070 nm and doubled 2140 nm components of the supercontinuum so that they are temporally coincident. An optical band-pass filter centered at 1070 nm selects the supercontinuum components required for self-referencing, shown in Fig. 2.3a, and impinging the filtered light on a photodetector reveals the carrier-envelope offset frequency of the EOM comb, shown in Fig. 2.2b. Note that downsampling introduces an ambiguity in the offset frequency due to the increased density of comb modes in the downsampled pulse train; this ambiguity can be removed by measuring the change in measured offset frequency with a change in  $f_{rep} = \omega_{rep}/2\pi$  provided by the synthesizer driving the modulators.

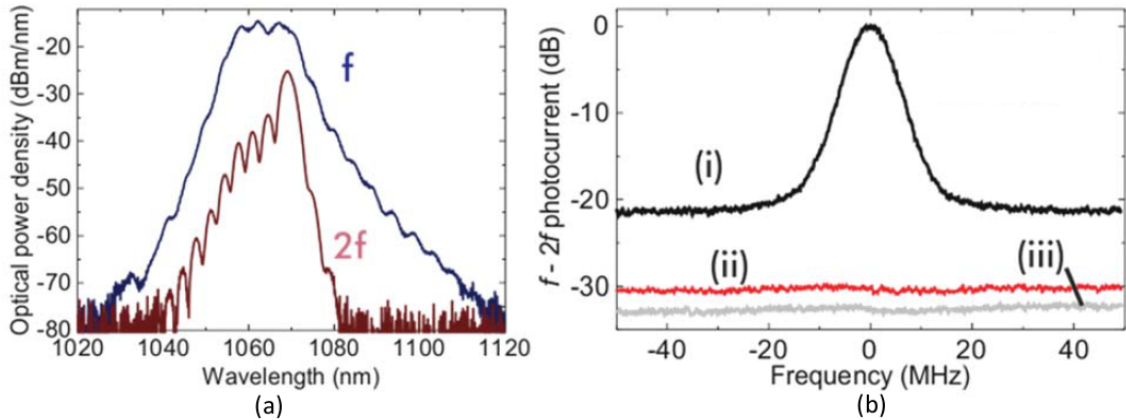


**Figure 2.3: Self-referencing of an EOM comb.** (a) Spectral components used for  $f - 2f$  self-referencing after passing through a 1070-nm optical bandpass filter: **native supercontinuum light (blue)** and **frequency-doubled 2140-nm supercontinuum light (red)** ARE THESE LABELED CORRECTLY. (b) Photodetected carrier-envelope offset frequency signal (black), along with a measurement of the intensity noise of the pulse train obtained by blocking one of the paths (red) and the photodetector noise floor (grey). **The intensity-noise measurement highlights the presence of a broad background noise floor on the  $f_0$  signal that must be the result of frequency fluctuations because it is not present when photodetecting either path alone.**

## 2.3 Noise considerations in EOM comb generation

An important difference between the EOM comb scheme and other approaches for generation of frequency combs is that the repetition rate is derived from a microwave source and is multiplied directly by a factor  $\mu$  to yield the frequency-comb mode with seed-laser-referenced mode number  $\mu$ . Therefore, the contribution to the frequency noise of mode  $\mu$  from the microwave source scales with the  $\mu$ , and the contribution to the power spectrum of frequency noise scales as  $\mu^2$ . This

presents a challenge in the generation of coherent supercontinuum light, where the modes relevant for  $f - 2f$  self-referencing are far from the seed laser and  $\mu$  is large. The factor by which the noise on the modulation tone  $f_{rep}$  is multiplied to determine its contribution to the noise on the measured carrier-envelope offset frequency is the ratio between the comb's carrier frequency (the frequency of the seed laser) and the repetition rate:  $\mu = f_c/f_{rep} = 19340$  for the 10 GHz comb discussed above (where  $f_c = 193.4$  THz for a 1550 nm seed laser). This contribution is shown in Fig. 2.4a, along with the contribution from the CW seed laser. The noise on  $f_{rep}$  results from technical noise on the synthesizer tone at low Fourier frequencies and approaches a white Johnson-Nyquist (thermal) phase-noise floor of -177 dBm/Hz at high Fourier frequencies. Noise in each of these regimes impacts the photodetected  $f_0$  signal: low-frequency noise contributes to the linewidth of the comb modes and therefore the  $f_0$  signal, while high-frequency noise contributes to a frequency-noise floor on the photodetected signal[95]. Unmitigated multiplication of this noise floor by the factor  $\mu^2 = 19340^2$  leads to a supercontinuum with optical frequency fluctuations that are large enough to prevent detection and measurement of  $f_0$ .

To address this problem and enable  $f - 2f$  self-referencing of our comb, we pass the comb through a Fabry-Perot filter cavity whose free-spectral range is actively stabilized to the comb's mode spacing. The filter cavity's Lorentzian transfer function reduces the optical frequency fluctuations of the comb modes at high frequency—these fluctuations are averaged over the photon lifetime of the cavity. This enables generation of a supercontinuum with resolvable modes that is suitable for  $f - 2f$  self-referencing and measurement of  $f_0$ .

The filter cavity used for this 10 GHz comb has a 7.5 MHz linewidth; equivalently, it has finesse of  $\mathcal{F} \sim 1333$ . The effect of passing the comb through the cavity is demonstrated concretely in Fig. 2.4b, where we compare the lineshape of a heterodyne beat between the supercontinuum and a CW laser with 1319 nm wavelength with and without the filter cavity in place. The signal-to-noise ratios for the beat with and without the filter cavity are 40 dB and 17 dB, respectively.

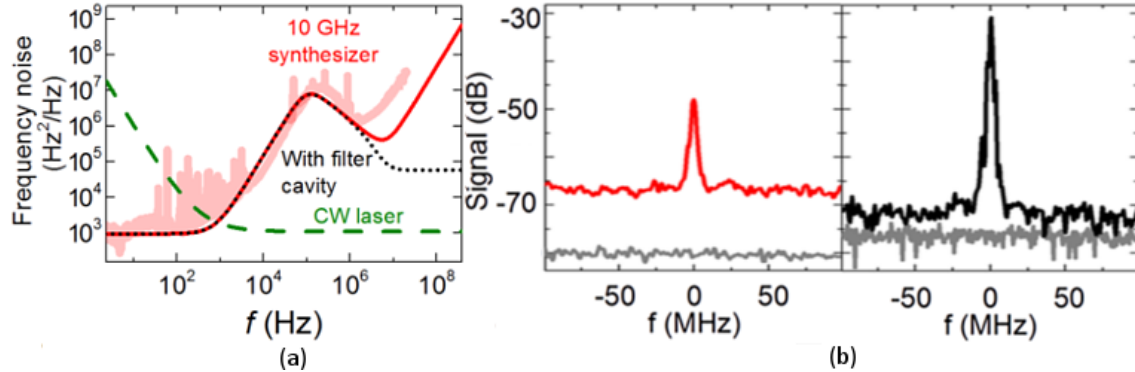


**Figure 2.4: Investigation of the noise properties of the EOM comb.** (a) Contributions to the frequency-noise spectrum of the carrier-envelope offset frequency: model of the input seed laser (dashed green), model of the 10 GHz synthesizer multiplied by  $19340^2$  without the filter cavity (solid red, experimental data thick red), and synthesizer multiplied by  $19340^2$  and the Lorentzian filter-cavity transfer function (dotted black). (b) Comparison of the detected beats between the supercontinuum and a CW laser with 1319 nm wavelength without (red, left) and with (black, right) the Fabry-Perot filter cavity. The level of intensity noise on the supercontinuum, measured by removing the 1319 nm CW laser, is shown by the lower gray trace in each plot; the elevated floor of the red trace relative to this background indicates that frequency noise is responsible for the reduced SNR of the beat without the filter cavity. Signal-to-noise ratios for the beat are 17 dB without and 40 dB with the filter cavity.

We also explore the effect of low-frequency fluctuations in the modulation tone  $f_{rep}$  by changing the source of this tone. The  $f_0$  signal shown in Fig. 2.3b is acquired with a tunable commercial

synthesizer providing  $f_{rep}$ . In Fig. 2.5 we show the detected  $f_0$  signal with a dielectric-resonator oscillator and a sapphire oscillator providing  $f_{rep}$ ; these sources have less low-frequency noise, and the effect of this lower noise is readily apparent in the reduced linewidth of the  $f_0$  signal. This indicates the importance of a high-performance microwave oscillator for future deployments of EOM combs.

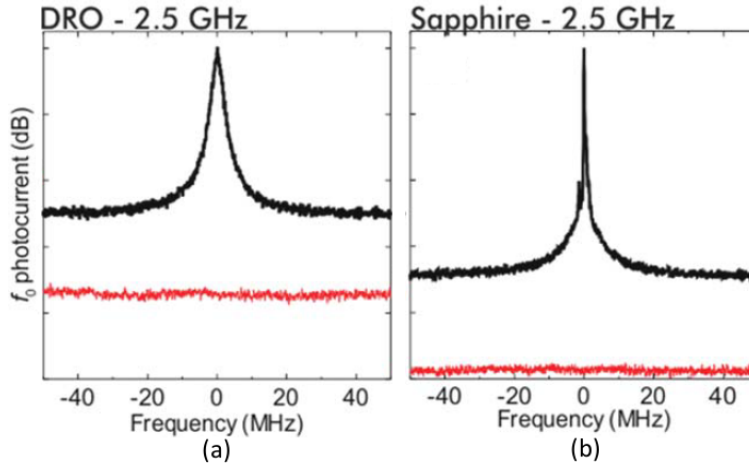


**Figure 2.5: Photodetected carrier-envelope-offset frequency signal with different sources for  $f_{rep}$ .** (a) The  $f_0$  beat resulting from a dielectric-resonator oscillator source for the modulation frequency. (b) Ibid with a sapphire oscillator as the source for  $f_{rep}$ , which has lower noise than both the tunable commercial synthesizer and the DRO. The reduction in linewidth associated with the change in the source for  $f_{rep}$  shows the effect of low-Fourier-frequency noise of  $f_{rep}$  on the frequency-noise characteristics of the EOM comb.

## 2.4 Outlook

The EOM comb approach for frequency-comb generation yields combs that are widely tunable and that can be flexibly tailored for specific applications. Because the comb generation is a non-resonant process (up to the optional inclusion of a filter cavity), the comb properties can be manipulated in real time with speed and range that greatly exceeds the capabilities of mode-locked lasers (where repetition-rate adjustment requires manipulation of moving parts) and microcombs (where repetition-rate control via phase modulation as described in Chap. ??, for example, is limited to the locking range afforded by the resonator dispersion). This has allowed, for example, the proposal and demonstration of ‘PHIRE’—Parallel Heterodyne Interferometry via Rep-rate Exchange—which is, essentially, dual-comb spectroscopy [Coddington2016] with a single frequency comb whose repetition-rate is periodically switched [Carlson2018].

Optica 3,  
414

EOM combs, with their lack of moving parts, also offer robust turn-key operation to a degree that is difficult to achieve with other comb sources. This has made them particularly promising for applications where long-term deployment with maximum up-time is important, such as calibration of astronomical spectrograms [Metcalf2018]. While the necessity of the filter cavity described here to enable  $f - 2f$  self-referencing is an apparent limitation, there are promising routes towards eliminating this requirement—using a high-power, tunable microwave oscillator could allow self-referencing of a repetition-rate-tunable EOM comb without a filter cavity.

CLEO2018  
JTh5A.1

## References

- [1] T. Udem, R. Holzwarth, and T. W. Hänsch. Optical frequency metrology. *Nature*, 416 (6877), **2002**, 233–237. DOI: [10.1038/416233a](https://doi.org/10.1038/416233a).
- [2] J. L. Hall. Nobel lecture: Defining and measuring optical frequencies. *Reviews of Modern Physics*, 78 (4), **2006**, 1279–1295. DOI: [10.1103/RevModPhys.78.1279](https://doi.org/10.1103/RevModPhys.78.1279).
- [3] T. W. Hänsch. Nobel lecture: Passion for precision. *Reviews of Modern Physics*, 78 (4), **2006**, 1297–1309. DOI: [10.1103/RevModPhys.78.1297](https://doi.org/10.1103/RevModPhys.78.1297).
- [4] J. K. Ranka, R. S. Windeler, and A. J. Stentz. Visible continuum generation in airsilica microstructure optical fibers with anomalous dispersion at 800 nm. *Optics Letters*, 25 (1), **2000**, 25. DOI: [10.1364/OL.25.000025](https://doi.org/10.1364/OL.25.000025).
- [5] T. Steinmetz, T. Wilken, C. Araujo-Hauck, R. Holzwarth, T. W. Hänsch, L. Pasquini, A. Manescau, S. D’Odorico, M. T. Murphy, T. Kentischer, W. Schmidt, and T. Udem. Laser frequency combs for astronomical observations. *Science*, 321 (5894), **2008**, 1335–7. DOI: [10.1126/science.1161030](https://doi.org/10.1126/science.1161030).
- [6] D. T. Spencer, T. Drake, T. C. Briles, J. Stone, L. C. Sinclair, C. Fredrick, Q. Li, D. Westly, B. R. Ilic, A. Bluestone, N. Volet, T. Komljenovic, L. Chang, S. H. Lee, D. Y. Oh, T. J. Kippenberg, E. Norberg, L. Theogarajan, M.-g. Suh, K. Y. Yang, H. P. Martin, K. Vahala, N. R. Newbury, K. Srinivasan, J. E. Bowers, S. A. Diddams, and S. B. Papp. An optical-frequency synthesizer using integrated photonics. *Nature*, 557, **2018**, 81–85. DOI: [10.1038/s41586-018-0065-7](https://doi.org/10.1038/s41586-018-0065-7).
- [7] R. W. Boyd. **Nonlinear Optics**. San Diego, CA: Elsevier, 2003.
- [8] T. J. Kippenberg, R. Holzwarth, and S. A. Diddams. Microresonator-Based Optical Frequency Combs. *Science (New York, N.Y.)*, 332 (6029), **2011**, 555–559. DOI: [10.1126/science.1193968](https://doi.org/10.1126/science.1193968).
- [9] A. A. Savchenkov, A. B. Matsko, and L Maleki. On Frequency Combs in Monolithic Resonators. *Nanophotonics*, 5, **2016**, 363–391. DOI: [10.1515/nanoph-2016-0031](https://doi.org/10.1515/nanoph-2016-0031).
- [10] Y. K. Chembo. Kerr optical frequency combs: Theory, applications and perspectives. *Nanophotonics*, 5 (2), **2016**, 214–230. DOI: [10.1515/nanoph-2016-0013](https://doi.org/10.1515/nanoph-2016-0013).
- [11] A. Pasquazi, M. Peccianti, L. Razzari, D. J. Moss, S. Coen, M. Erkintalo, Y. K. Chembo, T. Hansson, S. Wabnitz, P. Del’Haye, X. Xue, A. M. Weiner, and R. Morandotti. Micro-combs: A novel generation of optical sources. *Physics Reports*, 729, **2017**, 1–81. DOI: [10.1016/j.physrep.2017.08.004](https://doi.org/10.1016/j.physrep.2017.08.004).
- [12] E. Obrzud, S. Lecomte, and T. Herr. Temporal solitons in microresonators driven by optical pulses. *Nature Photonics*, 11 (August), **2017**, 600–607. DOI: [10.1038/nphoton.2017.140](https://doi.org/10.1038/nphoton.2017.140). arXiv: [1612.08993](https://arxiv.org/abs/1612.08993).
- [13] H. Lee, T. Chen, J. Li, K. Y. Yang, S. Jeon, O. Painter, and K. J. Vahala. Chemically etched ultrahigh-Q wedge-resonator on a silicon chip. *Nature Photonics*, 6 (6), **2012**, 369–373. DOI: [10.1038/nphoton.2012.109](https://doi.org/10.1038/nphoton.2012.109). arXiv: [1112.2196](https://arxiv.org/abs/1112.2196) (cited on page 1).

- [14] K. Y. Yang, K. Beha, D. C. Cole, X. Yi, P. Del'Haye, H. Lee, J. Li, D. Y. Oh, S. A. Diddams, S. B. Papp, and K. J. Vahala. Broadband dispersion-engineered microresonator on a chip. *Nature Photonics*, 10 (March), **2016**, 316–320. DOI: 10.1038/nphoton.2016.36.
- [15] G. P. Agrawal. **Nonlinear Fiber Optics**. 4th. Burlington, MA: Elsevier, 2007 (cited on page 15).
- [16] M. L. Calvo and V. Lakshminarayanan, eds. **Optical Waveguides: From Theory to Applied Technologies**. Boca Raton, FL: Taylor & Francis, 2007.
- [17] P. Del'Haye, S. A. Diddams, and S. B. Papp. Laser-machined ultra-high-Q microrod resonators for nonlinear optics. *Applied Physics Letters*, 102, **2013**, 221119 (cited on page 1).
- [18] A. N. Oraevsky. Whispering-gallery waves. *Quantum Electronics*, 32 (42), **2002**, 377–400. DOI: 10.1070/QE2001v031n05ABEH002205. arXiv: arXiv:1011.1669v3.
- [19] H. A. Haus. **Waves and Fields in Optoelectronics**. Englewood Cliffs: Prentice-Hall, 1984.
- [20] S. M. Spillane, T. J. Kippenberg, O. J. Painter, and K. J. Vahala. Ideality in a Fiber-Taper-Coupled Microresonator System for Application to Cavity Quantum Electrodynamics. *Physical review letters*, 91 (4), **2003**, 043902. DOI: 10.1103/PhysRevLett.91.043902.
- [21] V. S. Il'chenko and M. L. Gorodetskii. Thermal nonlinear effects in optical whispering gallery microresonators.pdf. *Laser Physics*, 2 (6), **1992**, 1004–1009.
- [22] T. Carmon, L. Yang, and K. J. Vahala. Dynamical thermal behavior and thermal self-stability of microcavities. *Optics Express*, 12 (20), **2004**, 4742–4750. URL: <http://www.ncbi.nlm.nih.gov/pubmed/19484026> <http://www.opticsinfobase.org/oe/abstract.cfm?uri=oe-12-20-4742>.
- [23] R. del Coso and J. Solis. Relation between nonlinear refractive index and third-order susceptibility in absorbing media. *Journal of the Optical Society of America B*, 21 (3), **2004**, 640. DOI: 10.1364/JOSAB.21.000640.
- [24] P. Del'Haye, A. Schliesser, O. Arcizet, T. Wilken, R. Holzwarth, and T. J. Kippenberg. Optical frequency comb generation from a monolithic microresonator. *Nature*, 450 (7173), **2007**, 1214–1217. DOI: 10.1038/nature06401.
- [25] T. Kippenberg, S. Spillane, and K. Vahala. Kerr-Nonlinearity Optical Parametric Oscillation in an Ultrahigh-Q Toroid Microcavity. *Physical Review Letters*, 93 (8), **2004**, 083904. DOI: 10.1103/PhysRevLett.93.083904.
- [26] A. A. Savchenkov, A. B. Matsko, D. Strekalov, M. Mohageg, V. S. Ilchenko, and L. Maleki. Low threshold optical oscillations in a whispering gallery mode CaF<sub>2</sub> resonator. *Physical Review Letters*, 93 (24), **2004**, 2–5. DOI: 10.1103/PhysRevLett.93.243905.
- [27] I. H. Agha, Y. Okawachi, M. A. Foster, J. E. Sharping, and A. L. Gaeta. Four-wave-mixing parametric oscillations in dispersion-compensated high- Q silica microspheres. *Physical Review A - Atomic, Molecular, and Optical Physics*, 76 (4), **2007**, 1–4. DOI: 10.1103/PhysRevA.76.043837.
- [28] T. Herr, V. Brasch, J. D. Jost, C. Y. Wang, N. M. Kondratiev, M. L. Gorodetsky, and T. J. Kippenberg. Temporal solitons in optical microresonators. *arXiv*, **2012**, 1211.0733. DOI: 10.1038/nphoton.2013.343. arXiv: 1211.0733.
- [29] T. Herr, V. Brasch, J. D. Jost, C. Y. Wang, N. M. Kondratiev, M. L. Gorodetsky, and T. J. Kippenberg. Temporal solitons in optical microresonators. *Nature Photonics*, 8 (2), **2014**, 145–152. DOI: 10.1109/CLEOE-IQEC.2013.6801769. arXiv: 1211.0733 (cited on page 3).
- [30] F. Leo, S. Coen, P. Kockaert, S.-P. Gorza, P. Emplit, and M. Haelterman. Temporal cavity solitons in one-dimensional Kerr media as bits in an all-optical buffer. *Nature Photonics*, 4 (7), **2010**, 471–476. DOI: 10.1038/nphoton.2010.120.

- [31] T. Herr, K. Hartinger, J. Riemensberger, C. Y. Wang, E. Gavartin, R. Holzwarth, M. L. Gorodetsky, and T. J. Kippenberg. Universal formation dynamics and noise of Kerr-frequency combs in microresonators. *Nature Photonics*, 6 (7), **2012**, 480–487. DOI: 10.1038/nphoton.2012.127.
- [32] Y. K. Chembo and C. R. Menyuk. Spatiotemporal Lugiato-Lefever formalism for Kerr-comb generation in whispering-gallery-mode resonators. *Physical Review A*, 87, **2013**, 053852. DOI: 10.1103/PhysRevA.87.053852.
- [33] S. Coen, H. G. Randle, T. Sylvestre, and M. Erkintalo. Modeling of octave-spanning Kerr frequency combs using a generalized mean-field Lugiato-Lefever model. *Optics letters*, 38 (1), **2013**, 37–39. URL: <http://www.ncbi.nlm.nih.gov/pubmed/23282830>.
- [34] M. Haelterman, S. Trillo, and S. Wabnitz. Dissipative modulation instability in a nonlinear dispersive ring cavity. *Optics Communications*, 91 (5-6), **1992**, 401–407. DOI: 10.1016/0030-4018(92)90367-Z.
- [35] T. Hansson, M. Bernard, and S. Wabnitz. Modulational Instability of Nonlinear Polarization Mode Coupling in Microresonators. 35 (4), **2018**. URL: <https://arxiv.org/pdf/1802.04535.pdf>. arXiv: arXiv:1802.04535v1.
- [36] Y. K. Chembo, I. S. Grudinin, and N. Yu. Spatiotemporal dynamics of Kerr-Raman optical frequency combs. *Physical Review A*, 92 (4), **2015**, 4. DOI: 10.1103/PhysRevA.92.043818.
- [37] C. Godey, I. V. Balakireva, A. Coillet, and Y. K. Chembo. Stability analysis of the spatiotemporal Lugiato-Lefever model for Kerr optical frequency combs in the anomalous and normal dispersion regimes. *Physical Review A*, 89 (6), **2014**, 063814. DOI: 10.1103/PhysRevA.89.063814.
- [38] I. V. Barashenkov and Y. S. Smirnov. Existence and stability chart for the ac-driven, damped nonlinear Schrödinger solitons. *Physical Review E - Statistical Physics, Plasmas, Fluids, and Related Interdisciplinary Topics*, 54 (5), **1996**, 5707–5725. DOI: 10.1103/PhysRevE.54.5707.
- [39] A. Coillet and Y. K. Chembo. Routes to spatiotemporal chaos in Kerr optical frequency combs. *Chaos*, 24 (1), **2014**, 5. DOI: 10.1063/1.4863298. arXiv: arXiv:1401.0927v1.
- [40] L. A. Lugiato and R. Lefever. Spatial Dissipative Structures in Passive Optical Systems. *Physical Review Letters*, 58 (21), **1987**, 2209–2211.
- [41] L. Lugiato and R. Lefever. Diffraction stationary patterns in passive optical systems. *Interaction of Radiation with Matter*, **1987**.
- [42] W. H. Renninger and P. T. Rakich. Closed-form solutions and scaling laws for Kerr frequency combs. *Scientific Reports*, 6 (1), **2016**, 24742. DOI: 10.1038/srep24742. arXiv: 1412.4164.
- [43] S. Coen and M. Erkintalo. Universal scaling laws of Kerr frequency combs. *Optics letters*, 38 (11), **2013**, 1790–1792. DOI: 10.1364/OL.38.001790. arXiv: arXiv:1303.7078v1.
- [44] Y. Wang, F. Leo, J. Fatome, M. Erkintalo, S. G. Murdoch, and S. Coen. Universal mechanism for the binding of temporal cavity solitons, **2017**, 1–10. URL: <http://arxiv.org/abs/1703.10604>. arXiv: 1703.10604 (cited on page 4).
- [45] P. Parra-Rivas, D. Gomila, P. Colet, and L. Gelens. Interaction of solitons and the formation of bound states in the generalized Lugiato-Lefever equation. *European Physical Journal D*, 71 (7), **2017**. DOI: 10.1140/epjd/e2017-80127-5. arXiv: arXiv:1705.02619v1 (cited on page 5).
- [46] V. Brasch, T. Herr, M. Geiselmann, G. Lihachev, M. H. P. Pfeiffer, M. L. Gorodetsky, and T. J. Kippenberg. Photonic chip-based optical frequency comb using soliton Cherenkov radiation. *Science*, 351 (6271), **2016**, 357. DOI: 10.1126/science.1253055. arXiv: 1410.8598.
- [47] X. Yi, Q.-F. Yang, K. Y. Yang, M.-G. Suh, and K. Vahala. Soliton frequency comb at microwave rates in a high-Q silica microresonator. *Optica*, 2 (12), **2015**, 1078–1085 (cited on page 3).

- [48] V. E. Lobanov, G. V. Lihachev, N. G. Pavlov, A. V. Cherenkov, T. J. Kippenberg, and M. L. Gorodetsky. Harmonization of chaos into a soliton in Kerr frequency combs. *Optics Express*, 24 (24), **2016**, 27382. DOI: 10.1126/science.aah4243. arXiv: 1607.08222.
- [49] C. Joshi, J. K. Jang, K. Luke, X. Ji, S. A. Miller, A. Klenner, Y. Okawachi, M. Lipson, and A. L. Gaeta. Thermally controlled comb generation and soliton modelocking in microresonators. *Optics Letters*, 41 (11), **2016**, 2565–2568. DOI: 10.1364/OL.41.002565. arXiv: 1603.08017.
- [50] W. Wang, Z. Lu, W. Zhang, S. T. Chu, B. E. Little, L. Wang, X. Xie, M. Liu, Q. Yang, L. Wang, J. Zhao, G. Wang, Q. Sun, Y. Liu, Y. Wang, and W. Zhao. Robust soliton crystals in a thermally controlled microresonator. *Optics Letters*, 43 (9), **2018**, 2002–2005. DOI: 10.1364/OL.43.002002.
- [51] H. Guo, M. Karpov, E. Lucas, A. Kordts, M. H. Pfeiffer, V. Brasch, G. Lihachev, V. E. Lobanov, M. L. Gorodetsky, and T. J. Kippenberg. Universal dynamics and deterministic switching of dissipative Kerr solitons in optical microresonators. *Nature Physics*, 13 (1), **2017**, 94–102. DOI: 10.1038/nphys3893. arXiv: 1601.05036.
- [52] J. K. Jang, M. Erkintalo, S. G. Murdoch, and S. Coen. Writing and erasing of temporal cavity solitons by direct phase modulation of the cavity driving field. *Optics Letters*, 40 (20), **2015**, 4755–4758. DOI: 10.1364/OL.40.004755. arXiv: 1501.05289.
- [53] J. K. Jang, M. Erkintalo, S. Coen, and S. G. Murdoch. Temporal tweezing of light through the trapping and manipulation of temporal cavity solitons. *Nature Communications*, 6, **2015**, 7370. DOI: 10.1038/ncomms8370. arXiv: 1410.4836.
- [54] Y. Wang, B. Garbin, F. Leo, S. Coen, M. Erkintalo, and S. G. Murdoch. Writing and Erasure of Temporal Cavity Solitons via Intensity Modulation of the Cavity Driving Field. *arXiv*, **2018**, 1802.07428. arXiv: 1802.07428.
- [55] S. B. Papp, K. Beha, P. Del'Haye, F. Quinlan, H. Lee, K. J. Vahala, and S. A. Diddams. Microresonator frequency comb optical clock. *Optica*, 1 (1), **2014**, 10–14. DOI: 10.1364/OPTICA.1.000010. arXiv: 1309.3525.
- [56] M. G. Suh, Q. F. Yang, K. Y. Yang, X. Yi, and K. J. Vahala. Microresonator soliton dual-comb spectroscopy. *Science*, 354 (6312), **2016**, 1–5. DOI: 10.1126/science.aah6516. arXiv: 1607.08222.
- [57] P. Marin-Palomo, J. N. Kemal, M. Karpov, A. Kordts, J. Pfeifle, M. H. Pfeiffer, P. Trocha, S. Wolf, V. Brasch, M. H. Anderson, R. Rosenberger, K. Vijayan, W. Freude, T. J. Kippenberg, and C. Koos. Microresonator-based solitons for massively parallel coherent optical communications. *Nature*, 546 (7657), **2017**, 274–279. DOI: 10.1038/nature22387. arXiv: 1610.01484.
- [58] J. D. Jost, T. Herr, C. Lecaplain, V. Brasch, M. H. P. Pfeiffer, and T. J. Kippenberg. Counting the cycles of light using a self-referenced optical microresonator. *Optica*, 2 (8), **2015**, 706–711. DOI: 10.1364/OPTICA.2.000706. arXiv: 1411.1354.
- [59] P. Del'Haye, A. Coillet, T. Fortier, K. Beha, D. C. Cole, K. Y. Yang, H. Lee, K. J. Vahala, S. B. Papp, and S. A. Diddams. Phase-coherent microwave-to-optical link with a self-referenced microcomb. *Nature Photonics*, 10 (June), **2016**, 1–5. DOI: 10.1038/nphoton.2016.105.
- [60] V. Brasch, E. Lucas, J. D. Jost, M. Geiselmann, and T. J. Kippenberg. Self-referenced photonic chip soliton Kerr frequency comb. *Light: Science & Applications*, 6 (1), **2017**, e16202. DOI: 10.1038/lsa.2016.202. arXiv: 1605.02801.
- [61] T. C. Briles, J. R. Stone, T. E. Drake, D. T. Spencer, C. Frederick, Q. Li, D. A. Westly, B. R. Illic, K. Srinivasan, S. A. Diddams, and S. B. Papp. Kerr-microresonator solitons for accurate carrier-envelope-frequency stabilization. *arXiv*, **2017**, 1711.06251. URL: <http://arxiv.org/abs/1711.06251>. arXiv: 1711.06251.

- [62] H. Taheri, A. A. Eftekhar, K. Wiesenfeld, and A. Adibi. Soliton formation in whispering-gallery-mode resonators via input phase modulation. *IEEE Photonics Journal*, 7 (2), **2015**, 2200309. DOI: 10.1109/JPHOT.2015.2416121.
- [63] J. R. Stone, T. C. Briles, T. E. Drake, D. T. Spencer, D. R. Carlson, S. A. Diddams, and S. B. Papp. Thermal and Nonlinear Dissipative-Soliton Dynamics in Kerr Microresonator Frequency Combs. *arXiv*, **2017**, 1708.08405. URL: <http://arxiv.org/abs/1708.08405>. arXiv: 1708.08405.
- [64] M. Zajnulina, M. Böhm, D. Bodenmüller, K. Blow, J. C. Boggio, A. Rieznik, and M. Roth. Characteristics and stability of soliton crystals in optical fibres for the purpose of optical frequency comb generation. *Optics Communications*, 393 (November 2016), **2017**, 95–102. DOI: 10.1016/j.optcom.2017.02.035 (cited on page 1).
- [65] A. Haboucha, H. Leblond, M. Salhi, A. Komarov, and F. Sanchez. Coherent soliton pattern formation in a fiber laser. *Optics Letters*, 33 (5), **2008**, 524–526. DOI: 10.1364/OL.33.000524 (cited on page 1).
- [66] F. Amrani, M. Salhi, P. Grelu, H. Leblond, and F. Sanchez. Universal soliton pattern formations in passively mode-locked fiber lasers. *Optics letters*, 36 (9), **2011**, 1545–1547. DOI: 10.1364/OL.36.001545 (cited on page 1).
- [67] A. Haboucha, H. Leblond, M. Salhi, A. Komarov, and F. Sanchez. Analysis of soliton pattern formation in passively mode-locked fiber lasers. *Physical Review A*, 78, **2008**, 043806. DOI: 10.1103/PhysRevA.78.043806 (cited on page 1).
- [68] B. A. Malomed, A Schwache, and F Mitschke. Soliton lattice and gas in passive fiber-ring resonators. *Fiber and Integrated Optics*, 17 (4), **1998**, 267–277. DOI: 10.1080/014680398244867 (cited on page 1).
- [69] F. Mitschke and A. Schwache. Soliton ensembles in a nonlinear resonator. *Journal of Optics B: Quantum and Semiclassical Optics*, 10 (6), **1998**, 779–788 (cited on page 1).
- [70] A. Schwache and F. Mitschke. Properties of an optical soliton gas. *Physical Review E*, 55 (6), **1997**, 7720–7725. DOI: 10.1103/PhysRevE.55.7720 (cited on page 1).
- [71] H. A. Haus and W. Huang. Coupled-Mode Theory. *Proceedings of the IEEE*, 79 (10), **1991**, 1505–1518. DOI: 10.1109/5.104225 (cited on page 3).
- [72] T. Herr, V. Brasch, J. D. Jost, I. Mirgorodskiy, G. Lihachev, M. L. Gorodetsky, and T. J. Kippenberg. Mode Spectrum and Temporal Soliton Formation in Optical Microresonators. *Physical Review Letters*, 113 (12), **2014**, 123901. DOI: 10.1103/PhysRevLett.113.123901 (cited on page 3).
- [73] Y. Liu, Y. Xuan, X. Xue, P.-H. Wang, S. Chen, A. J. Metcalf, J. Wang, D. E. Leaird, M. Qi, and A. M. Weiner. Investigation of mode coupling in normal-dispersion silicon nitride microresonators for Kerr frequency comb generation. *Optica*, 1 (3), **2014**, 137–144. DOI: 10.1364/OPTICA.1.000137 (cited on page 3).
- [74] T. Hansson and S. Wabnitz. Bichromatically pumped microresonator frequency combs. *Physical Review A*, 90, **2014**, 013811. DOI: 10.1103/PhysRevA.90.013811. arXiv: 1404.2792 (cited on page 5).
- [75] D. V. Skryabin and W. J. Firth. Interaction of cavity solitons in degenerate optical parametric oscillators. *Optics letters*, 24 (15), **1999**, 1056–1058. DOI: 10.1364/OL.24.001056. arXiv: 9906004 [patt-sol] (cited on page 5).
- [76] S. Wabnitz. Control of soliton train transmission, storage, and clock recovery by cw light injection. *Journal of the Optical Society of America B*, 13 (12), **1996**, 2739–2749. URL: <http://www.scopus.com/inward/record.url?eid=2-s2.0-0030378988&partnerID=tZ0tx3y1> (cited on page 5).

- [77] J. A. Barker and D. Henderson. What is "liquid"? Understanding the states of matter. *Reviews of Modern Physics*, 48 (4), **1976**, 587–671. DOI: 10.1103/RevModPhys.48.587 (cited on page 7).
- [78] T. Egami and S. Billinge. **Underneath the Bragg Peaks**. 2nd. Oxford, UK: Elsevier, 2012, p. 422 (cited on page 7).
- [79] N. W. Ashcroft and D. N. Mermin. **Solid State Physics**. 1st ed. Belmont, CA: Brooks/Cole, 1976, p. 826 (cited on page 9).
- [80] A. Weiner. **Ultrafast Optics**. 1st ed. Hoboken, NJ: Wiley, 2009, p. 598 (cited on page 11).
- [81] T. Kobayashi, T. Sueta, Y. Cho, and Y. Matsuo. High-repetition-rate optical pulse generator using a Fabry-Perot electro-optic modulator. *Applied Physics Letters*, 21 (8), **1972**, 341–343. DOI: 10.1063/1.1654403 (cited on page 13).
- [82] M. Kourogi, K. Nakagawa, and M. Ohtsu. Wide-Span Optical Frequency Comb Generator for. 29 (10), **1993** (cited on page 13).
- [83] H. Murata, A. Morimoto, T. Kobayashi, and S. Yamamoto. Optical pulse generation by electrooptic-modulation method and its application to integrated ultrashort pulse generators. *IEEE Journal of Selected Topics in Quantum Electronics*, 6 (6), **2000**, 1325–1331. DOI: 10.1109/2944.902186 (cited on page 13).
- [84] T. Sakamoto, T. Kawanishi, and M. Izutsu. frequency comb generation using a Mach Zehnder. *Optics Letters*, 32 (11), **2007**, 1515–1517 (cited on page 13).
- [85] I. Morohashi, T. Sakamoto, H. Sotobayashi, T. Kawanishi, I. Hosako, and M. Tsuchiya. Widely repetition-tunable 200 fs pulse source using a Mach-Zehnder-modulator-based flat comb generator and dispersion-flattened dispersion-decreasing fiber. *Optics letters*, 33 (11), **2008**, 1192–1194. DOI: 10.1364/OL.33.001192 (cited on page 13).
- [86] A. Ishizawa, T. Nishikawa, A. Mizutori, H. Takara, S. Aozasa, A. Mori, H. Nakano, A. Takada, and M. Koga. Octave-spanning frequency comb generated by 250 fs pulse train emitted from 25 GHz externally phase-modulated laser diode for carrier-envelope-offset-locking. *Electronics Letters*, 46 (19), **2010**, 1343. DOI: 10.1049/el.2010.2228 (cited on page 13).
- [87] R. Wu, V. R. Supradeepa, C. M. Long, D. E. Leaird, and A. M. Weiner. Generation of very flat optical frequency combs from continuous-wave lasers using cascaded intensity and phase modulators driven by tailored radio frequency waveforms. *Optics Letters*, 35 (19), **2010**, 3234. DOI: 10.1364/OL.35.003234. arXiv: 1005.5373 (cited on page 13).
- [88] V. R. Supradeepa and A. M. Weiner. Bandwidth scaling and spectral flatness enhancement of optical frequency combs from phase-modulated continuous-wave lasers using cascaded four-wave mixing. *Optics Letters*, 37 (15), **2012**, 3066. DOI: 10.1364/OL.37.003066 (cited on page 13).
- [89] A. J. Metcalf, V. Torres-company, D. E. Leaird, S. Member, A. M. Weiner, and A. Broadband. High-Power Broadly Tunable Electrooptic Frequency Comb Generator. *IEEE Journal of Selected Topics in Quantum Electronics*, 19 (6), **2013**, 3500306. URL: <http://ieeexplore.ieee.org/stamp/stamp.jsp?arnumber=65553388> (cited on page 13).
- [90] R. Wu, V. Torres-company, D. E. Leaird, and A. M. Weiner. Optical Frequency Comb Generation. 21 (5), **2013**, 6045–6052. DOI: 10.1364/OE.21.006045 (cited on page 13).
- [91] J. M. Dudley, G. G. Genty, and S. Coen. Supercontinuum generation in photonic crystal fiber. *Reviews of Modern Physics*, 78 (4), **2006**, 1135–1184. DOI: 10.1103/RevModPhys.78.1135 (cited on page 15).
- [92] A. M. Weiner. Femtosecond pulse shaping using spatial light modulators. *Review of Scientific Instruments*, 71 (5), **2000**, 1929–1960. DOI: 10.1063/1.1150614 (cited on page 15).
- [93] K. Beha, D. C. Cole, P. Del'Haye, A. Coillet, S. A. Diddams, and S. B. Papp. Electronic synthesis of light. *Optica*, 4 (4), **2017**, 406–411. DOI: 10.1364/OPTICA.4.000406 (cited on page 16).

- [94] a. a. Amorim, M. V. Tognetti, P Oliveira, J. L. Silva, L. M. Bernardo, F. X. Kärtner, and H. M. Crespo. Sub-two-cycle pulses by soliton self-compression in highly nonlinear photonic crystal fibers. *Optics letters*, 34 (24), **2009**, 3851–3853. doi: 10.1364/OL.34.003851 (cited on page 17).
- [95] G. Di Domenico, S. Schilt, and P. Thomann. Simple approach to the relation between laser frequency noise and laser line shape. *Applied optics*, 49 (25), **2010**, 4801–4807. doi: 10.1364/AO.49.004801 (cited on page 18).
- [96] S. Backus, C. G. Durfee, M. M. Murnane, and H. C. Kapteyn. High power ultrafast lasers. *Review of Scientific Instruments*, 69 (3), **1998**, 1207. doi: 10.1063/1.1148795.
- [97] A. Baltuska, M. Uiberacker, E. Goulielmakis, R. Kienberger, V. S. Yakovlev, T. Udem, T. W. Hänsch, and F. Krausz. Phase-Controlled Amplification of Few-Cycle Laser Pulses. *IEEE Journal of Selected Topics in Quantum Electronics*, 9 (4), **2003**, 972–989.
- [98] C. Gohle, J. Rauschenberger, T. Fuji, T. Udem, A. Apolonski, F. Krausz, and T. W. Hänsch. Carrier envelope phase noise in stabilized amplifier systems. 30 (18), **2005**, 2487–2489.
- [99] J. Rauschenberger, T. Fuji, M. Hentschel, A.-J. Verhoef, T. Udem, C. Gohle, T. W. Hänsch, and F. Krausz. Carrier-envelope phase-stabilized amplifier system. *Laser Physics Letters*, 3 (1), **2006**, 37–42. doi: 10.1002/lapl.200510053.
- [100] M. E. Fermann, V. I. Kruglov, B. C. Thomsen, J. M. Dudley, and J. D. Harvey. Self-similar propagation and amplification of parabolic pulses in optical fibers. *Physical review letters*, 84 (26 Pt 1), **2000**, 6010–3. url: <http://www.ncbi.nlm.nih.gov/pubmed/10991111>.
- [101] M. Hirano, T. Nakanishi, T. Okuno, and M. Onishi. Silica-Based Highly Nonlinear Fibers and Their Application. *Sel. Top. Quantum Electron.*, 15 (1), **2009**, 103–113. doi: 10.1109/JSTQE.2008.2010241.
- [102] D. Mandridis, I. Ozdur, F. Quinlan, M. Akbulut, J. J. Plant, P. W. Juodawlkis, and P. J. Delfyett. Low-noise, low repetition rate, semiconductor-based mode-locked laser source suitable for high bandwidth photonic analog digital conversion. *Applied Optics*, 49 (15), **2010**, 2850–2857.
- [103] H.-A. Bachor and P. J. Manson. Practical Implications of Quantum Noise. *Journal of Modern Optics*, 37 (11), **1990**, 1727–1740. doi: 10.1080/09500349014551951.
- [104] F. Quinlan, T. M. Fortier, H. Jiang, and S. a. Diddams. Analysis of shot noise in the detection of ultrashort optical pulse trains. *Journal of the Optical Society of America B*, 30 (6), **2013**, 1775. doi: 10.1364/JOSAB.30.001775.
- [105] D. C. Cole, K. M. Beha, S. A. Diddams, and S. B. Papp. Octave-spanning supercontinuum generation via microwave frequency multiplication. *Proceedings of the 8th Sympson on Frequency Standards and Metrology 2015, Journal of Physics: Conference Series*, 723, **2016**, 012035. doi: 10.1088/1742-6596/723/1/012035.
- [106] A. M. Heidt. Efficient Adaptive Step Size Method for the Simulation of Supercontinuum Generation in Optical Fibers. *Journal of Lightwave Technology*, 27 (18), **2009**, 3984–3991.
- [107] J. Hult. A Fourth-Order Runge-Kutta in the Interaction Picture Method for Simulating Supercontinuum Generation in Optical Fibers. *Journal of Lightwave Technology*, 25 (12), **2007**, 3770–3775. doi: 10.1109/JLT.2007.909373.
- [108] R. Driad, J. Rosenzweig, R. E. Makon, R. Lösch, V. Hurm, H. Walcher, and M. Schlechtweg. InP DHBT-Based IC Technology for 100-Gb / s Ethernet. *IEEE Trans. on Electron. Devices*, 58 (8), **2011**, 2604–2609.
- [109] D. Ferenci, M. Grozing, M. Berroth, R. Makon, R. Driad, and J. Rosenzweig. A 25 GHz Analog Demultiplexer with a Novel Track and Hold Circuit for a 50 GS / s A / D-Conversion System in InP DHBT Technology. In: **Microwave Symposium Digest**. 2012, pp. 1–3.